Towards the nonlinear acousto-magneto-plasmonics

2016 J. Opt. 18 093002

(http://iopscience.iop.org/2040-8986/18/9/093002)

IOP Publishing Journal of Optics
J. Opt. 18 (2016) 093002 (19pp) doi:10.1088/2040-8978/18/9/093002

Topical Review

Towards the nonlinear acousto-magneto-plasmonics

Vasily V Temnov[1,2], Ilya Razdolski[2], Thomas Pezeril[1], Denys Makarov[3], Denis Seletskiy[4], Alexey Melnikov[2] and Keith A Nelson[5]

[1] IMMM CNRS 6283, Université du Maine, F-72085 Le Mans cedex, France
[2] Fritz-Haber-Institut der MPG, Phys. Chemie, Faradayweg 4-6, D-14195 Berlin, Germany
[3] Helmholtz-Zentrum Dresden-Rossendorf e. V., Institute of Ion Beam Physics and Materials Research, D-01328 Dresden, Germany
[4] Department of Physics and Center for Applied Photonics, University of Konstanz, D-78457 Konstanz, Germany
[5] Department of Chemistry, Massachusetts Institute of Technology, Cambridge, MA 02139, USA

E-mail: vasily.temnov@univ-lemans.fr

Received 9 May 2015, revised 21 June 2016
Accepted for publication 27 June 2016
Published 2 August 2016

Abstract

We review the recent progress in experimental and theoretical research of interactions between the acoustic, magnetic and plasmonic transients in hybrid metal-ferromagnet multilayer structures excited by ultrashort laser pulses. The main focus is on understanding the nonlinear aspects of the acoustic dynamics in materials as well as the peculiarities in the nonlinear optical and magneto-optical response. For example, the nonlinear optical detection is illustrated in detail by probing the static magneto-optical second harmonic generation in gold–cobalt–silver trilayer structures in Kretschmann geometry. Furthermore, we show experimentally how the nonlinear reshaping of giant ultrashort acoustic pulses propagating in gold can be quantified by time-resolved plasmonic interferometry and how these ultrashort optical pulses dynamically modulate the optical nonlinearities. An effective medium approximation for the optical properties of hybrid multilayers enables the understanding of novel optical detection techniques. In the discussion we also highlight recent works on the nonlinear magneto-elastic interactions, and strain-induced effects in semiconductor quantum dots.

Keywords: acousto-plasmonics, magneto-plasmonics, magneto-acoustics, nonlinear optics, nonlinear acoustics, ultrafast spectroscopy in condensed matter, hybrid nanophotonics

(Some figures may appear in colour only in the online journal)

1. Motivation

The main objective of this review is to summarize recent developments in understanding nonlinear interactions in magneto-plasmonic and acousto-plasmonic multilayer structures. We aim to provide a clear overview of these fundamental interactions governing the macroscopic properties of these complex multilayer structures excited by femtosecond laser pulses. The role of the ultrashort laser pulses is twofold. On the one hand, high peak intensity is advantageous for efficient excitation of nonlinear optical processes such as second and third harmonic generation. On the other hand, short laser pulses enable excitation of electronic, acoustic and magnetic transients, as well as allow the sampling of the ensuing dynamics in pump-probe experiments. In addition to the application of an external magnetic field, which provides active control of the static and dynamic properties in condensed matter systems, in this review we emphasize the high potential that nanoscale acoustic pulses offer for study, as well as selective dynamic control of various degrees of

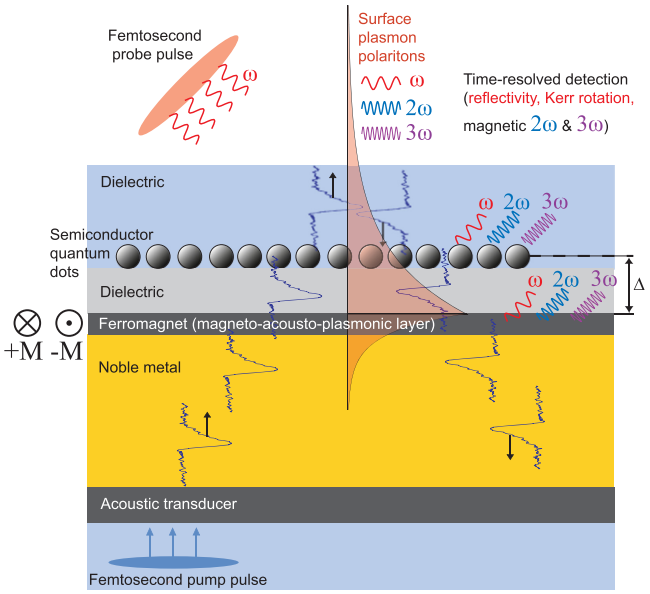

Figure 1. Schematic of a prototypical device for studies of the magneto-acousto-plasmonic response of various material systems (e.g. semiconductor quantum dots) under femtosecond excitation and external magnetic field. Ultrafast pump pulse excites a structure made from acoustic transducer, noble metal and a ferromagnet and the ensuing dynamics is probed via various detection methods reviewed here. Figure reproduced with permission from [8]

freedom in complex matter. As we outline below, the functional metallic multilayers are particularly attractive for these tasks as they support excitation and propagation conditions for ultrashort acoustic pulses while at the same time offer strong sub-micrometer confinement of surface-plasmon-polaritons (SPPs). In turn, macroscopic propagation of SPPs in nanolayers for distances exceeding tens of micrometers makes it possible to enhance the nonlinear light-matter interactions in such systems.

A prototypical experimental setup showing the concepts outlined above is schematically depicted in figure 1. A femtosecond pump pulse excites the nanolayer structure, which is comprised of an acoustic transducer, noble metal and ferromagnetic layer, while under an optional (arbitrary oriented) static magnetic field. Magnetic, acoustic and plasmonic transient(s) can be used to study ultrafast dynamics in the quantum-optical system of interest, which is embedded into a dielectric cap layer in close proximity (at a distance Δ) to the metal-dielectric interface [1, 2]. The two examples that we motivate here are (i) the control of the magneto-optical properties in a ferromagnetic compound and (ii) time-domain studies of semiconductor quantum dots (QDs) under strong transient acoustic strain bias at the nanoscale. The response of these systems can be detected via the reviewed methods, such as magnetic second harmonic generation (mSHG), time-resolved plasmonic and nonlinear optical (second and third harmonic) probing.

While the structure presented in figure 1 has not yet been realized, we hope to convince the reader of its great potential for scientific investigations of magneto-acousto-plasmonic interactions in various nanoscale systems. As such, this review provides a progress report on the recent studies which address various isolated components or ideas, comprising potential building blocks toward our envisioned device.

The Review is divided into several sections. Section two discusses two experimental geometries used to excite surface plasmon polaritons in magneto-plasmonic multilayers: (i) Kretschmann configuration for a thin multilayer on a dielectric prism and (ii) the plasmonic interferometry for macroscopically thick metallic multilayers.

Section three describes some recent advances in the linear and nonlinear magneto-plasmonics. A weak external magnetic field is shown to induce large modulation in the intensity of surface second harmonic generation (SHG) and also to identify the role of surface plasmon polaritons in the nonlinear frequency conversion phenomena. The effective medium approximation for magneto-plasmonic metal-ferromagnet multilayer structures helps to understand the results. A phenomenological model based on the interference between the magnetic and nonmagnetic contributions from two effective interfaces is developed to explain the observations. Section four discusses generation and characterization of giant and ultrashort acoustic pulses in (noble metal)-ferromagnet bilayer structures and highlights their impact on the SHG output. Another phenomenological model based on the acoustic modulation of the optical properties of a thin ferromagnetic layer is proposed to explain the experimental observations.

Section five concerns the specificity of the sample fabrication for plasmonic and acoustic measurements, with the main focus on the growth conditions and microscopic characterization of multilayer structures.

In the discussion section we outline other involved phenomena, notably related to ultrafast magnetization dynamics, thermal effects and strain effects in semiconductor QDs.

2. Optical spectroscopy with surface plasmon polaritons

Time-dependent perturbations of electron density distribution in metals are at the heart of plasmonics [3–7]. The time-dependent response is governed by oscillations of the electrons at the so-called plasma frequency, which, in the long-wavelength limit of free-electron approximation, is given by $\omega_{\mathrm{p}} = \sqrt{\frac{n_e e^2}{\varepsilon_0 m}}$, where n_e, e and m are the electronic density, charge and mass, respectively and ε_0 is the dielectric permittivity of free space. Since in most metals there is at least one free electron per ion, the resulting electron plasma density is very high, $n_e \sim 10^{22}\,\mathrm{cm}^{-3}$, with a corresponding ω_{p} in the visible to ultraviolet frequency range. Optical fields at frequency $\omega < \omega_{\mathrm{p}}$ are effectively screened by the plasma, resulting in a penetration profile which is exponentially attenuated within the so-called *skin depth* δ_{skin}. For the majority of metals the skin depth lies in the range of 10–20 nm in the visible and near-infrared frequency range [9]. A Drude model provides the dielectric response function of free electrons

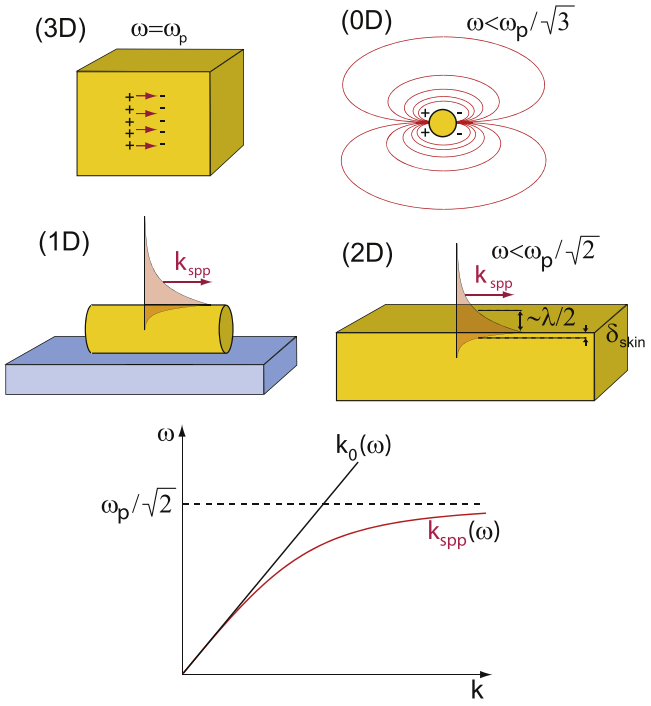

Figure 2. Frequency of oscillations of electron gas in bulk metal (3D), is modified by surface effects in metallic nanoparticles (0D), nanowires (1D) and surfaces (2D). Whereas metallic nanoparticles possess a specific, localized surface plasmon (LSP) resonance frequency determined by their geometry, surface plasmon polaritons (SPPs) in 1D and 2D form a broad frequency band $\omega(k_{spp})$ and may propagate over macroscopic distances while obeying a characteristic dispersion relation. SPP wavevector $k_{spp}(\omega)$ is always larger than wavevector of plane electromagnetic waves in vacuum $k_0(\omega)$ at the same frequency.

$\varepsilon_m(\omega) = 1 - \omega_p^2/(\omega(\omega + i/\tau_c))$, where τ_c stands for an effective electron scattering time. This simple expression offers a reasonable approximation for the optical properties of free-carrier-like metals (Al, Ag, Au, Cu) used in plasmonics because of their small losses (large τ_c).

In low-dimensional metallic nanostructures such as metal surfaces (2D), wires (1D) or dots (0D), the frequency of plasma oscillations is substantially affected by charge separation at the surface. This is illustrated in figure 2 which shows the different plasma frequencies and mixed electromagnetic/surface charge density excitations in various geometries.

In the case of zero-dimensionality (0D), the electron gas oscillates at a fixed resonance frequency and may lead to significant enhancement of optical fields close to the surface of the nanoparticle due to the nanoantenna effect. This field enhancement is of key importance to understanding the interaction mechanisms between plasmonic nanoparticles and nano-scale light emitters [10, 11]. The resonance frequency for metal nanoparticles of the diameter smaller than the skin depth δ_{skin} tends to a value of $\omega_p/\sqrt{3}$, while with the increased diameter it experiences a red shift [12]. By varying the diameter of 0D metallic nanoparticles ranging from a few to tens of nanometers, this localized plasmon frequency can be tuned over the entire visible spectral range.

In addition to the bulk and the localized plasmon modes, surface plasmon modes can be supported at one or two dimensional interfaces. These collective excitations are known as surface plasmon polaritons. These are coupled electromagnetic—surface charge density waves on metal surfaces, gratings and wires which can propagate over macroscopic distances of tens of micrometers, largely exceeding the optical wavelength λ. In the case of metallic surface, the electromagnetic fields in the direction normal to the interface are exponentially bound. On the vacuum side, the typical exponential decay length is a fraction of λ, therefore resulting in strong sub-wavelength field confinement. Inside the metal, the intensity of electric and magnetic components of the electromagnetic field decays exponentially within the skin depth. SPPs exist in a broad frequency band below the cut-off frequency $\omega_p/\sqrt{2}$ and are characterized by dispersion relation $\omega(k_{spp})$, where k_{spp} is the wave vector of the surface plasmon (lower panel in figure 2). This dispersion relation is identical for 1D and 2D cases, as long as the nanowire radius significantly exceeds the skin depth [13] and is given by $k_{spp}(\omega) = k_0(\omega)\sqrt{\frac{\varepsilon_m(\omega)}{\varepsilon_m(\omega)+1}}$, where $k_0(\omega) = \omega/c$ is the wave vector of light in vacuum and we assumed an SPP propagating along the free-standing nanowire in air. In practice, as sketched in figure 2, nanowires are often deposited on dielectric substrates [1, 14, 15] and the (1D) SPP dispersion in asymmetric dielectric environment splits in several branches demonstrating a more complex behavior [16, 17].

The details of the coupling of the surface plasmon modes and optical fields in low-dimensional structures are worth further consideration. Due to the localized nature of the 0D resonance, plasmonic response of the metallic nanoparticles can be effectively approximated as a Hertzian dipole, where large spatial bandwidth of the possible wave vectors manifests in direct coupling to plane electromagnetic waves. The situation is entirely different for surface plasmon polaritons in 1D and 2D geometries. Since their dispersion curve $\omega(k_{spp})$ never crosses the light line in vacuum ($k_{spp} > k_0$ for all frequencies), these modes cannot be excited by plane electromagnetic waves impinging on a metal–air interface. An elegant and most widely used way to excite SPP modes is provided by the so-called Kretschmann geometry (see figure 3), where a thin metal film deposited on top of a dielectric prism is illuminated by a collimated light beam through the prism with refractive index $n > 1$. For a particular combination of the incident angle θ_0 and light frequency ω_0, the in-plane component of the wave vector of incident light $k_x(\omega, \theta) = n(\omega)k_0(\omega)\sin\theta$ matches the wave vector of a surface plasmon polariton:

$$k_{spp}(\omega_0) = n(\omega_0)k_0(\omega_0)\sin\theta_0. \quad (1)$$

In case of a monochromatic laser source, the angular dependence of reflectivity $R(\theta)$ shows a sharp dip at $\theta = \theta_0$ indicating that a significant fraction of the incident energy is converted into the SPP mode, propagating along the metal-air interface. The metal layer should be relatively thin (typically ~50 nm) in order to allow for efficient coupling of the

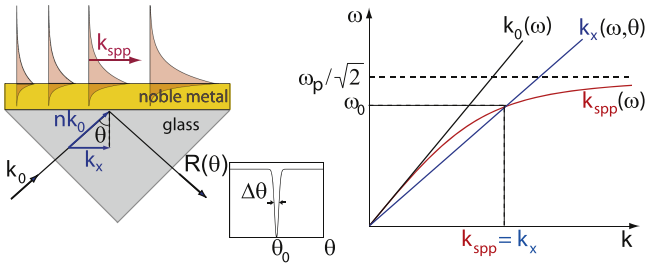

Figure 3. Illumination of a thin (noble) metal film through the glass prism (known as Kretschmann geometry [18]) supports the conditions for excitation of the surface plasmon polariton modes. SPP excitation at the metal-air interface is manifested by a sharp minimum in the reflectivity $R(\theta)$ around the resonant angle θ_0. The condition is satisfied at the intersection point of the dispersion relations of the light and surface plasmon modes ($k_{spp}(\omega_0) = k_x(\omega_0, \theta_0)$ on the right panel), resulting in a strong electric field enhancement at the surface and the excitation of light waves at the metal-air interface.

incident light from the glass-metal to the the metal-air interface. Thicker films would decrease the coupling efficiency due to enhanced attenuation of the evanescent wave in metal whereas in even thinner films the hybridization of the SPPs at the two interfaces and the subsequent formation of symmetric and antisymmetric modes would introduce additional radiative losses [19]. Upon satisfaction of the SPP excitation condition, the intensity of the excited SPP mode grows with propagation along the illuminated region of the surface and can get up to 300 times larger as compared to the incident wave, limited by the ohmic losses in the metal film [20, 21]. In practice, this field enhancement is lower due to parasitic effects which reduce the surface plasmon propagation length such as, for example, surface roughness and material inhomogeneities [22]. In hybrid ferromagnet-(noble metal) multilayer structures the field enhancement is further reduced due to SPP absorption in a ferromagnet.

Scattering of the incident light on natural or artificial surface defects, with a size of the order of a wavelength or smaller, represents another common way to satisfy the condition for SPP excitation [24]. A pair of appropriately spaced sub-wavelength defects can serve for in- and outcoupling of the incident light to the SPP modes and producing the plasmonic interference fringes [23, 25–27].

Figure 4(a) shows a scanning electron microscope (SEM) micrograph of the plasmonic microinterferometer, which consists of a slit-groove pair milled into a 200 nm gold film with a 30 kV Ga^+ focused ion beam. The 200 nm gold film was grown by magnetron sputtering on a 2 nm thin chromium buffer layer on a glass substrate. The length of both the slit and the groove is 50 μm. The slit has a width of 100 nm and extends through the thickness of the gold layer to the glass substrate. The depth of the groove is 100 nm and it is 200 nm wide. A series of similar structures was fabricated, where the slit-groove tilt angle was systematically varied between 3° and 15° and the slit-groove distance between 0 and 50 μm. If the whole area of the microinterferometer is homogeneously illuminated with coherent light, the SPP, first launched at the groove, will propagate toward the slit and interfere with the

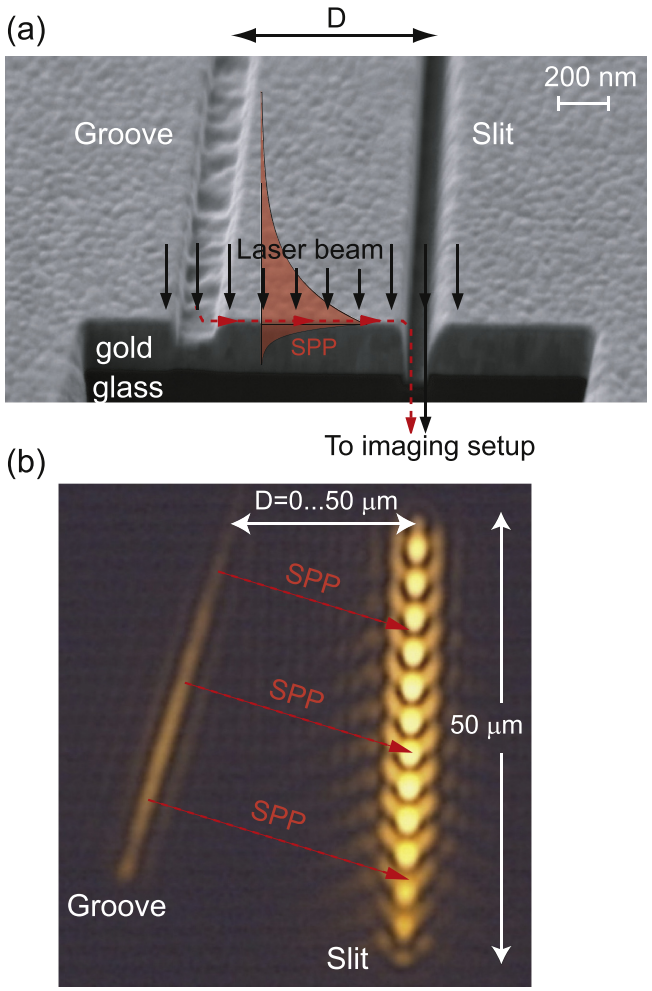

Figure 4. Plasmonic microinterferometer based on a tilted slit-groove pair. (a) SEM micrograph showing a typical depth profile of the slit-groove structure (slit-groove distance D of 1 μm, slit-groove tilt angle of 3°, slit width 100 nm, groove width 200 nm, groove depth 100 nm) milled into a 200 nm thick gold film on a glass substrate by a focused ion beam. (b) False-color image of optical transmission of a homogeneously illuminated microinterferometer in a near-infrared, with a minimum slit-groove spacing of $D = 20$ μm and slit-groove tilt angle of 15°. The periodic modulation of light intensity transmitted through the slit is due to interference with surface plasmons launched by the groove (see text for details). Adopted with permission from [23].

directly transmitted light upon outcoupling back into the light mode. An optical transmission image of a slit-groove microinterferometer, illuminated by a collimated p-polarized laser beam (beam waist ~40 μm FWHM, $\lambda = 800$ nm) under nearly normal incidence, is shown in figure 4(b). A bright periodic intensity modulation of light transmitted through the slit represents the plasmonic interference pattern. A small tilt angle between the slit and the groove determines the spatial fringe periodicity and allows for interferometric measurements at a single wavelength with a single structure.

The interferometric sensitivity to the phase shift acquired by the SPP upon macroscopic propagation of the distance between the groove and the slit can be harnessed for sensing. In the hybrid multilayers, the phase and/or the contrast of

these plasmonic interference fringes can be conveniently controlled via the modulation of the dielectric susceptibility by means of either magneto-optical effects in magneto-plasmonics or elasto-optical effects in acousto-plasmonics, both effects with relative modulation of the transmitted light intensity below 1%.

3. Magneto-plasmonics

3.1. Linear magneto-plasmonics

The influence of the external magnetic field on plasmonic properties is extensively discussed elsewhere [28]. The magnetic field control of the plasmonic properties has been demonstrated in a number of systems [29–42]. Here we shall focus on the properties of the SPPs in a hybrid (noble) metal-ferromagnet-(noble) metal multilayer structure, which has been proven as a strong playground for magneto-plasmonics [7, 43, 44] (figure 5). The geometry of SPPs at 800 nm wavelength in a Au–Co–Au multilayer structure is shown in figure 5(a). Both the real and imaginary parts of the complex SPP wave vector can be calculated within the effective medium approximation [44, 45]. The effective dielectric function

$$\varepsilon_{\text{eff}} = \frac{1}{\delta_{\text{skin}}}\int_0^{\infty} \varepsilon(z)\mathrm{e}^{-z/\delta_{\text{skin}}}\mathrm{d}z, \tag{2}$$

accurately reproduces the SPP dispersion relation in a magneto-plasmonic multilayer structure

$$k_{\text{spp}} = k_0\sqrt{\frac{\varepsilon_{\text{eff}}}{1+\varepsilon_{\text{eff}}}}. \tag{3}$$

The validity of this approximation is illustrated by the dependence of SPP propagation length $L_{\text{spp}} = 1/(2\text{Im}[k_{\text{spp}}])$ in a Au–Co–Au multilayer, where the 6 nm thick cobalt layer was placed at a variable depth h below the gold–air interface (figure 5(b)). A good quantitative agreement between the effective medium approximation and exact transfer-matrix calculations [46] is obtained. A significant decrease of the SPP propagation length L_{spp} for small values of h is attributed to additional ohmic losses introduced when the ferromagnetic layer is in a non-negligible overlap with the spatial envelope of the intensity profile associated with the SPP mode. The influence of a thin ferromagnetic layer on the skin depth δ_{skin} in a hybrid noble metal-ferromagnet-noble metal multilayer is negligibly small and one can safely use its value for SPPs propagating at the noble metal-dielectric interface.

The effective medium approximation provides an adequate description of the dependence of SPP wave vector on the magnetic field as well. Assuming that the magnetization vector $\overrightarrow{M}$ is pointing along the y-direction the effective magneto-optical tensor is given by:

$$\hat{\varepsilon}_{\text{eff}}(\pm m_y) = \begin{pmatrix} \varepsilon_{\text{eff}} & 0 & \pm\varepsilon^{xz}_{\text{eff}} m_y \\ 0 & \varepsilon_{\text{eff}} & 0 \\ \mp\varepsilon^{xz}_{\text{eff}} m_y & 0 & \varepsilon_{\text{eff}} \end{pmatrix}, \tag{4}$$

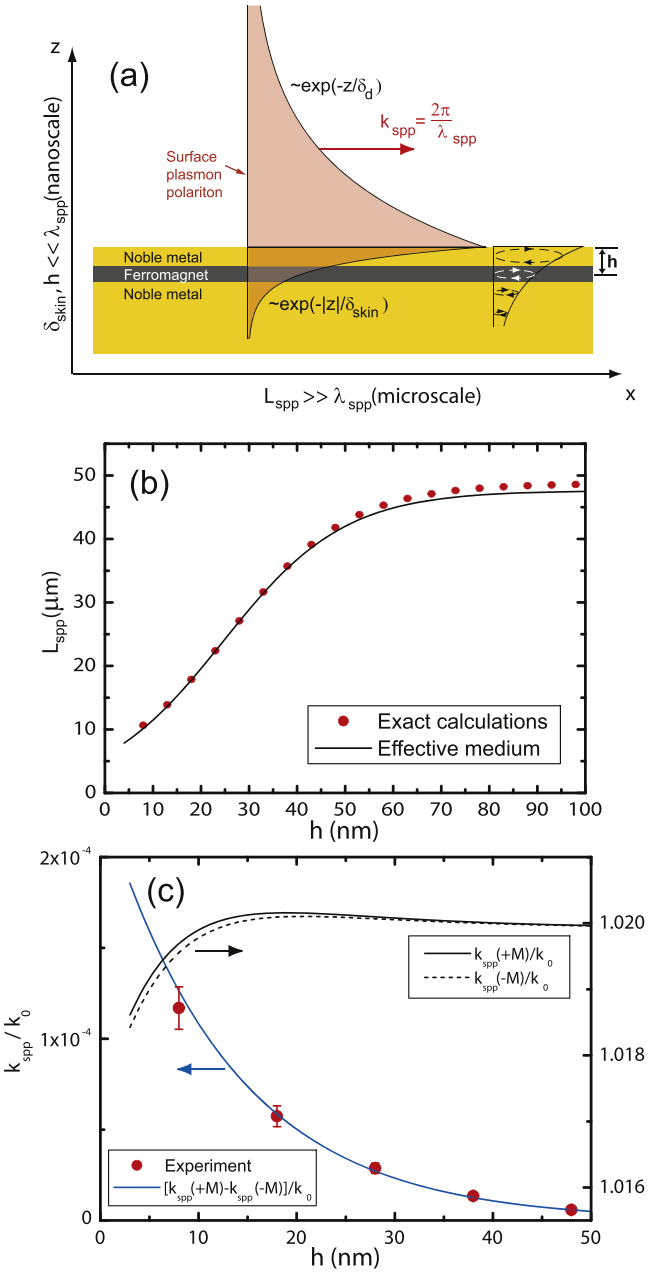

Figure 5. (a) SPPs in metal/ferromagnet/metal multilayer structures possess the spatial distribution of the in-plane electric field (shaded area shows $|E_z(z)|^2$), which is almost identical to that for a single metal film. Dashed elliptical contours represent the shape of the SPP electric field driving the motion of the electrons. (b) The dependence of the SPP decay length L_{spp} on the location h of the cobalt layer beneath the gold–air interface, showing excellent agreement with an effective medium approximation (black line). (c) In-plane magnetization reversal (in y-direction) in ferromagnetic cobalt changes the SPP wave vector $k_{\text{spp}}(\pm M)$. Its magnetic modulation $k_{\text{spp}}(+M) - k_{\text{spp}}(-M)$ obtained within the effective medium approximation is in agreement with experimental measurements from [44]. Figure (a) adopted with permission from [7].

with $m_y = M_y/M_S$ (normalized to the saturation magnetization M_S) and the non-diagonal components

$$\varepsilon^{xz}_{\text{eff}} = \frac{1}{\delta_{\text{skin}}}\int_0^{\infty} \varepsilon^{xz}(z)\mathrm{e}^{-z/\delta_{\text{skin}}}\mathrm{d}z, \tag{5}$$

we obtain the following dispersion relation for SPPs [47]:

$$k_{\mathrm{spp}}(\pm m_y) = k_0\sqrt{\frac{\varepsilon_{\mathrm{eff}}}{1+\varepsilon_{\mathrm{eff}}}}\left(1 \pm \frac{\mathrm{i}\varepsilon^{xz}_{\mathrm{eff}} m_y}{(1-\varepsilon^2_{\mathrm{eff}})\sqrt{\varepsilon_{\mathrm{eff}}}}\right). \quad (6)$$

For a special case of a ferromagnet (FM) layer with thickness $h_1 \ll \delta_{\mathrm{skin}}$ sandwiched between two layers of a noble metal, the effective medium approximation for the non-diagonal dielectric susceptibility component gives

$$\varepsilon^{xz}_{\mathrm{eff}} \simeq \frac{h_1}{\delta_{\mathrm{skin}}}\varepsilon^{xz}_{(\mathrm{FM})}\mathrm{e}^{-h/\delta_{\mathrm{skin}}} \quad (7)$$

resulting in the following magneto-plasmonic modulation Δk_{mp} of SPP wave vector:

$$\Delta k_{\mathrm{mp}} \simeq \mathrm{i}\varepsilon^{xz}_{(\mathrm{FM})} m_y \frac{2h_1\varepsilon_{\mathrm{eff}}k_0^2}{(1+\varepsilon_{\mathrm{eff}})(1-\varepsilon^2_{\mathrm{eff}})}\mathrm{e}^{-h/\delta_{\mathrm{skin}}}. \quad (8)$$

Here we have used the expression for SPP skin depth $\delta_{\mathrm{skin}} = \frac{1}{2k_0}\mathrm{Im}\frac{\sqrt{1+\varepsilon_{\mathrm{eff}}}}{\varepsilon_{\mathrm{eff}}}$ introduced the magnetic modulation of SPP wave vector $2\Delta k_{\mathrm{mp}} = k_{\mathrm{spp}}(+m_y) - k_{\mathrm{spp}}(-m_y)$. It is worth noting that this result is identical to the analytical expression obtained from transfer-matrix calculations for the limit of an infinitely thin ferromagnetic layer [44, 46]. Figure 5(c) compares the results of this analytical approach with the experimentally observed magneto-plasmonic modulation of SPP wave vector in a Au/Co/Au trilayer structure induced by a weak periodic external magnetic field with an amplitude of 20 mT [44], i.e. upon the in-plane magnetization switching: $k_{\mathrm{spp}}(\pm M) \equiv k_{\mathrm{spp}}(m_y = \pm 1)$.

The developed theoretical approach appears to be useful not only in the interferometric measurements with SPPs, but also in the conventional Kretschmann geometry. In a Au/Co/Ag multilayer the SPP resonance can be excited at both 800 and 400 nm wavelengths, figure 6(a). The SPP dispersion in figure 6(b) is displayed by the shaded area where the width is proportional to SPP damping (imaginary part of SPP wave vector), which strongly increases when approaching the blue part of the visible spectral range. Whereas SPP dispersion results in the shift of the SPP resonance angle θ_0 for 400 nm light (as compared to 800 nm), the increased damping makes the Kretschmann reflectivity dip much broader (figure 6(c)).

The effect of the external magnetic field is the same for both frequencies and leads to a small shift of the resonance angles upon magnetization reversal. The positions of the Kretschmann reflectivity minima precisely correspond to the zeros on magneto-plasmonic modulation curves, confirming the physical interpretation suggesting that the magneto-plasmonic modulation of SPP wave vector should result in an angular shift of the reflectivity minima (see figure 6(c)).

Here we would like to note that the reflectivity minimum in Kretschmann configuration cannot always be attributed to the excitation of SPPs. The dispersion of surface electromagnetic waves obeying the boundary conditions may depend on the direction of the perpendicular energy flow inside a thin metal film [19]. Whereas the energy flow from the top to the bottom (i.e. from the metal-air to the metal-dielectric interface) corresponds to the propagation of damped SPP modes, in the opposite case (energy flow from the bottom to the top) results in the excitation of the so-called perfectly absorbed (PA) mode. The difference in dispersion relations between an SPP and a PA mode (the latter corresponds to the reflectivity minimum in Kretschmann configuration) has been experimentally observed only recently [48]. In the forthcoming discussion of the nonlinear magneto-plasmonic response we leave the question about possible contributions of PA modes at the frequency 2ω open.

As we are going to show in the forthcoming sections, the effective medium approximation for SPPs, which was originally introduced in the linear magneto-plasmonics, appears to be also useful for the nonlinear magneto-plasmonics and acousto-plasmonics.

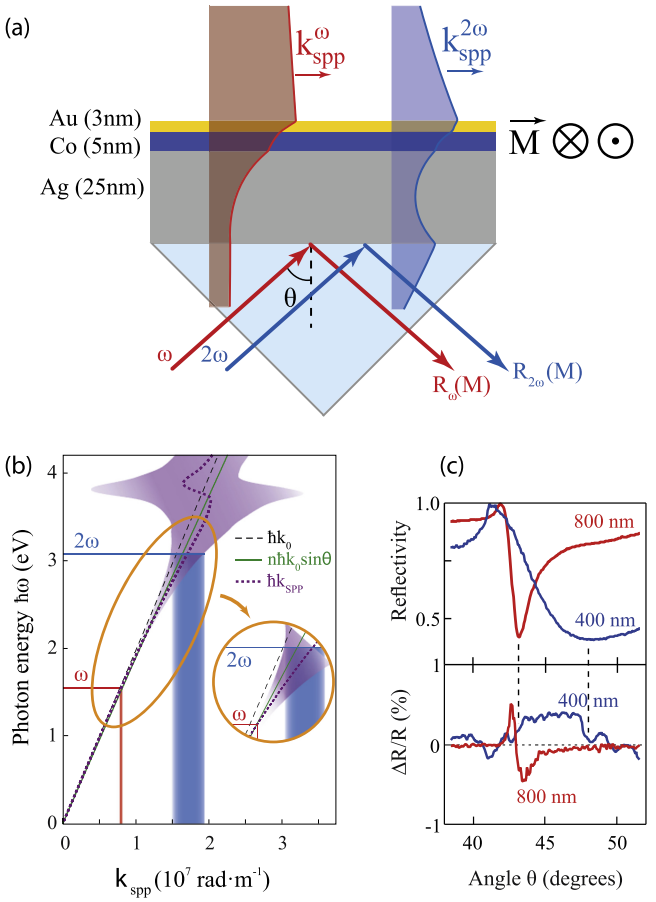

Figure 6. (a) Surface plasmons in thin Au/Co/Ag multilayer structures: the calculated spatial distribution of the squared tangential projection of SPPs-electric field at the fundamental ω and double 2ω frequencies at their resonant angles. (b) Dispersion of the SPP in the Au/Co/Ag trilayer under study. Black dash and green solid lines represent the photon dispersion in vacuum and in glass, respectively. Thick dot purple line is the analytically calculated SPP dispersion, its linewidth is shown with the purple background area. The inset illustrates the possibility of a simultaneous excitation of the SPPs at both frequencies ω and 2ω. (c) Linear-optical reflectivity R and magnetization-induced reflectivity variations $\Delta R/R = 2[R(+M) - R(-M)]/[R(+M) + R(-M)]$ for the excitation with the 800 and 400 nm wavelength. Figure adopted with permission from [45].

3.2. Nonlinear magneto-plasmonics

Nonlinear magneto-plasmonics is a relatively young field of magneto-photonics, which utilizes SPP excitations for tailoring the magnetization-induced contributions to the nonlinear-optical response of systems. The motivation for the emergence of this field of research is essentially twofold. First, as compared with nonlinear plasmonics [4, 5, 27], magnetic field conveniently offers a universal tool for controlling the nonlinear-optical response. Second, nonlinear magneto-optical effects are much stronger as compared to their linear counterparts, where magnetization-induced effects stay relatively small despite of being enhanced by SPPs [45, 49].

As it has been discussed in the previous section, in linear magneto-plasmonics the magnetic effects in the transversal Kerr geometry (magnetization is perpendicular to the incidence plane) are usually ascribed to the magnetization-induced modulation of SPP wave vector k_{spp}. However, in the nonlinear magneto-optics the response is more complex. In what follows, we shall restrict our considerations of nonlinear optical effects to SHG only, although the general principles of nonlinear magneto-plasmonics also apply to other effects such as difference frequency (often in THz domain), third harmonic generation, etc. Here we focus on the advantages of the SPP-induced SHG in magnetic media, including both enhancement of the magnetic effects and unraveling new SPP-assisted mechanisms to control optical nonlinearities.

One of the basic nonlinear-optical processes, SHG is governed by the second-order nonlinear-optical susceptibility tensor $\chi^{(2)}$. Various mechanisms of the anharmonicity in the optical response to electromagnetic field $E(\omega)$ lead to the emergence of the second-order nonlinear polarization at the double frequency 2ω [50]:

$$P_i(2\omega) = \chi^{(2)}_{ijk}(-2\omega;\, \omega,\, \omega) : E_j(\omega)E_k(\omega). \qquad (9)$$

This polarization then emits an electromagnetic wave. One of the key properties of the $\chi^{(2)}$ tensor is its strong sensitivity to the inversion symmetry. It can be shown that dipolar $\chi^{(2)}$ vanishes in the centrosymmetric media such as, for instance, bulk metals. In such systems efficient SHG is generated predominantly at the interfaces, where the inversion symmetry is broken. Under resonant excitation conditions in Kretschmann configuration SPPs boost up the local electromagnetic fields and can strongly enhance the SHG output [51]. In certain cases it is also convenient to take into account the influence of SPPs in the form of a resonant contribution to the $\chi^{(2)}$-tensor [50, 52]. Importantly, since $\chi^{(2)}(-2\omega;\, \omega,\, \omega)$ is sensitive to resonances (of various nature) not only at the fundamental ω, but also at the double frequency 2ω, SPPs at both of these frequencies contribute to the SHG output [53, 54].

Within this formalism, the magnetization-induced modulation of the SHG output is described in the following way. In magnetized media, the magnetization-dependent $\chi^{(2)}$ tensor can be represented as a sum of the non-magnetic (crystallographic) $\chi^{(2)}$ and magnetization-induced $\pm\chi^{(2,m)}$ contributions [55]. The latter changes sign upon reversing the magnetization, whereas the interference of these two contributions results in a magnetization-induced modulation of the SHG intensity (figure 7(a)). The magnitude of the effect can be conveniently characterized by the so-called magnetic SHG (mSHG) contrast $\rho_{2\omega}$:

$$\rho_{2\omega} = \frac{I_{2\omega}(+M) - I_{2\omega}(-M)}{I_{2\omega}(+M) + I_{2\omega}(-M)}, \qquad (10)$$

where $I_{2\omega}(+M)$ and $I_{2\omega}(-\mathrm{M})$ are the SHG intensities measured for the two opposite directions of magnetization. It should be noted that in a complex multilayer system, where multiple SHG sources are located at each interface, the rigorous description of the SHG output becomes increasingly complicated.

Due to a large number of the non-zero $\chi^{(2)}$ components, whose magnitudes and phases are *a priori* unknown, the approach we propose here refrains from taking into account all of them. Instead, the *effective interface* approximation treats effective $\chi^{(2)}$ at the two interfaces as unknown fit parameters (figure 7(b)). Within this approach, the role of SPP excitation in altering the magnetization-induced effects in SHG can be considered twofold. Upon such an excitation,

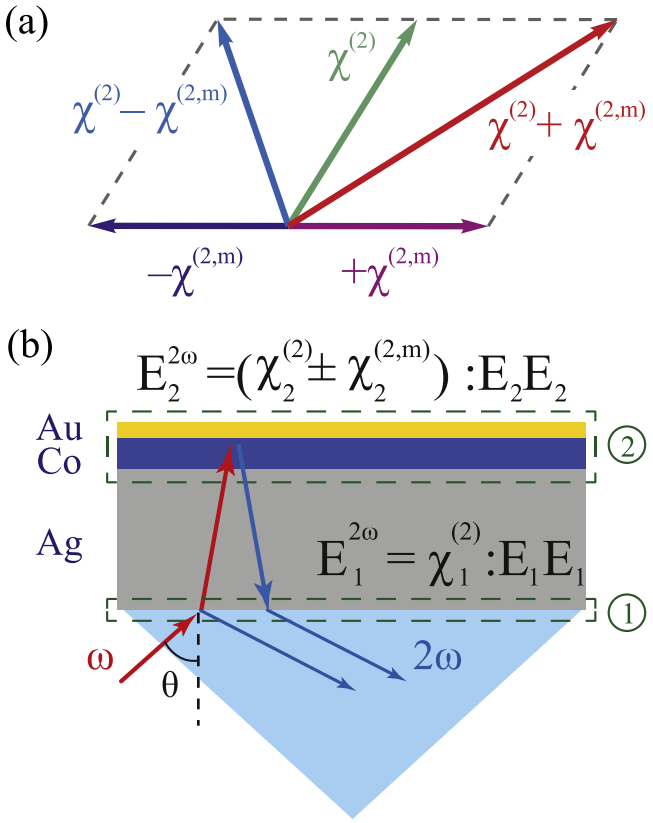

Figure 7. (a) Illustration of the origin of the inequality of the SHG intensities for the opposite direction of the magnetization M leading to the non-zero magnetic SHG contrast $\rho_{2\omega}$. The sign of the magnetic contribution to the nonlinear susceptibility $\pm\chi^{(2,m)}$ is flipped when the magnetization is reversed. (b) Magnetic SHG generation in a multilayer structure excited in Kretschmann geometry: SHG sources at the two *effective interfaces* marked by dashed contours: bottom (1, glass/Ag) and top (2, air/Au/Co/Ag) within the effective medium (*effective interface*) approximation.

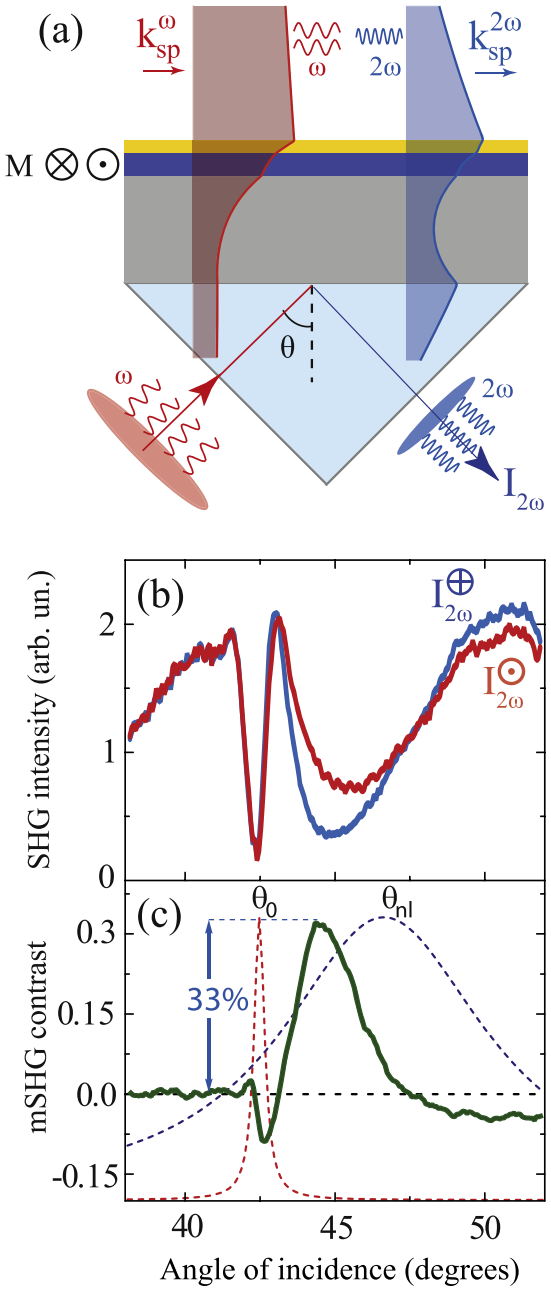

Figure 8. (a) Schematic of the SPP-induced magnetic SHG in Kretschmann geometry. The shaded areas represent the calculated distributions of the square of the SPP electric field $|E_z|^2$. A noticeable field enhancement at the air/Au interface indicates that the SPPs at both ω and 2ω are excited. Angular dependence of (b) the SHG intensity for the two opposite directions of magnetization in Co (red and blue) and (c) mSHG magnetic contrast (green). Red and blue dashed lines represent the SPP resonance lines for the 800 nm pump wavelength (described by equation (1)) and the nonlinear (SHG) excitation at 400 nm wavelength (according to equation (11), respectively. Note that the maximum of mSHG contrast is located between fundamental and the nonlinear (SHG) SPP resonances.

either the relative magnitude of the $\chi^{(2)}$ contributions or the relative phase between them can be modulated. The former, realized by Krutyanskiy *et al* [56] relies on the tensorial nature of $\chi^{(2)}$. Here, the crystallographic and magnetic SHG contributions are provided by the different projections of the fundamental field $E(\omega)$. These projections experience unequal SPP-assisted enhancement resulting in a modulation of the magnetization-induced SHG output. The second option [57, 58] highlighted the importance of the SPP-induced variations of the phase of the electromagnetic field. The physical origin of such phase modulations beyond the usual field enhancement remains largely unexplored.

A number of systems has been successfully investigated with nonlinear magneto-plasmonics. We note that nonlinear magneto-optics of nanoparticles and planar nanostructures [59–62] supporting localized surface plasmon resonances are beyond the scope of this work. The most straightforward approach utilizing SPP excitation at the interface of a ferromagnetic (Fe, Co, Ni) rather than conventional plasmonic (Al, Ag, Au, Co) metals faces a few challenges. Apart from dealing with overdamped plasmonic excitations ($L_{spp} < \lambda_{spp}$), these metals possess a relatively low second-order nonlinearity usually attributed to the localized *d*-band electrons. Nevertheless, magnetic SHG studies both on periodically perforated films [57] and in Kretschmann geometry [63] demonstrated significant SPP-assisted modulation of the magnetic contrast $\rho_{2\omega}$. In the systems discussed above, the incident electromagnetic wave excited SPPs at the fundamental frequency ω and the plasmonic enhancement of the local electromagnetic field $E(\omega)$ boosted the efficiency of the nonlinear-optical conversion.

Multilayer structures consisting of a ferromagnetic layer sandwiched between the two layers of noble metals offer a considerable expansion of opportunities in nonlinear magneto-plasmonics. For example, photons initially up-converted (frequency-doubled) at the interfaces can excite SPPs at 2ω and thus contribute to the enhancement of the SHG output [54, 64]. This mechanism requires the sample to support propagating SPP modes at the double frequency 2ω. It can be especially challenging in the case of SPP excitation on periodically corrugated surfaces, where the spatial periodicity was designed to achieve resonant conditions for SPP excitation at the fundamental frequency ω only. Another drawback is related to increased optical losses caused by the spectral overlap of SPP at 2ω with interband transitions, which is the case for Au at photon energies above 2.4 eV. This shifted the focus of attention toward other plasmonic metals such as Al or Ag which are capable of sustaining SPPs across the whole visible spectral range [65–68].

In the following we discuss a showcase of the proposed nonlinear magneto-plasmonic mechanism where a significant improvement of the magnetization-induced modulation reaching up to 33% has been achieved. We consider a thin gold/cobalt/silver trilayer grown on a glass substrate by means of the magnetron sputtering. A 5 nm thin magneto-optically active layer of ferromagnetic cobalt was protected from oxidation by a 3 nm thin layer of gold. A 25 nm thick silver layer acted as the main constituent in this hybrid plasmonic nanostructure, which was excited by 100 fs short laser pulses through the glass prism. The laser beam was focused into a spot of approximately 50 μm in diameter by means of a lens with 150 mm focal distance, resulting in the angular excitation width of about 1°. The reflected SHG

intensity was recorded as a function of the incidence angle θ for the two opposite directions of magnetization in cobalt in the transverse Kerr geometry (see figure 8(a)).

Due to the dispersion in equation (1), the SPP excitations at fundamental and double frequencies in Kretschmann geometry occur at slightly different angles. However, nonlinear-optical considerations discussed above suggest a possibility of nonlinear phase-matching between the second harmonic SPP at the gold–air interface with the k-vector $k_{\mathrm{spp}}^{2\omega}$ and the excitation source at the silver-glass interface characterized by the in-plane component of the k-vector $n(\omega)k_0(\omega)\sin\theta$. This phase-matching occurs at an angle θ_{nl} given by:

$$k_{\mathrm{spp}}^{2\omega} = 2n(\omega)k_0(\omega)\sin\theta_{\mathrm{nl}}. \tag{11}$$

Being just one of several possible SPP frequency conversion pathways [64, 69], this phase-matching condition is of paramount importance as it determines the resonant SPP-induced enhancement of the nonlinear susceptibility $\chi^{(2)} = \chi^{(2)}_{\mathrm{nr}} + \chi^{(2)}_{\mathrm{res}}(\theta)$ with SPP-mediated resonant contribution [50, 52]:

$$\chi^{(2)}_{\mathrm{res}}(\theta) \propto \frac{1}{\theta - \theta_{\mathrm{nl}} + \mathrm{i}\Gamma} \tag{12}$$

with $\Gamma = \mathrm{Im}[k_{\mathrm{spp}}^{2\omega}]/(k_0(\omega)n(\omega))$.

Whereas the linear reflectivity at both frequencies ω and 2ω shows only small modulations of the order of 1%, as discussed in the previous section (figure 6(c)), the angular dependence of the nonlinear SHG spectra in figure 8(b) displays drastic changes. Contrary to the previously reported results on a gold film [54], the angular positions of SPP resonances for the fundamental and SHG frequencies in our multilayer structure correspond to the pronounced minima in the SHG intensity. A strong dependence of the total SHG intensity on the magnetization direction $I_{2\omega}(\pm M)$ is quantified by the magnetic SHG contrast $\rho_{2\omega}$ shown in figure 8(c).

It is seen that the largest magnetization-induced modulation of the SHG intensity is accompanied by the SPP excitation at the SHG frequency and not the fundamental one. We note that the largest mSHG contrast is observed in between of the linear and nonlinear SPP excitation angles, while decreasing almost to zero at the two resonances. The latter is likely to happen due to the 90° phase shift between the magnetic and non-magnetic SHG contributions at the resonances, driven by the SPP electromagnetic field distribution. Angular dependence of mSHG contrast displays a large modulation amplitude reaching 33% at $\theta = 44°$. The data for other excitation wavelengths can be found elsewhere [45]. For the shortest wavelength (760 nm) the mSHG maximum is only about 20%, since in this case the SPP damping at the SHG frequency becomes so large that the system approaches the region with the non-propagating (overdamped) SPPs.

Note that the mSHG contrast at the fundamental SPP resonance is barely reaching 10%. This observation is in line with the most recent results by Zheng *et al* [63], who reported similar values of the mSHG contrast on a 10 nm thin iron film on glass, as well as with the results by Pavlov *et al* [70] obtained on Au/Co/Au multilayer, the structures not supporting SPPs at the SHG frequency. This fact, along with the dispersive shift of mSHG maximum reinforces our conclusion that the 33% large mSHG contrast (which is equivalent to the increase of the SHG intensity by a factor of 2 upon magnetization reversal) is dominated by the nonlinear SPP resonance at the SHG frequency.

Following Palomba and Novotny [54], the complex angular dependence of the SHG intensity from a thin gold film on glass is explained by an interference of two contributions coming from the metal-air and metal-glass interfaces. In our case (figure 7(b)) the silver-glass interface acts as a source of the nonmagnetic SHG $\vec{E}_1^{\,2\omega}$, and the upper part consisting of Au and Co layers is assumed to generate the electric field $\vec{E}_2^{\,2\omega}$ containing both magnetic $\chi^{(2\,m)}$ and nonmagnetic $\chi^{(2)}$ contributions. Thus the total SHG intensity $I_{2\omega}$ is described by:

$$\begin{aligned} I_{2\omega} &\propto |\vec{E}_1^{\,2\omega} + \vec{E}_2^{\,2\omega} \pm \vec{E}_{2m}^{\,2\omega}| \\ &= |\chi_1^{(2)} : \vec{E}_1\vec{E}_1 + (\chi_2^{(2)} \pm \chi_2^{(2m)}) : \vec{E}_2\vec{E}_2|^2. \end{aligned} \tag{13}$$

Here the complex tensor components $\chi_1^{(2)}$ and $\chi_2^{(2)} \pm \chi_2^{(2m)}$ represent the effective optical nonlinearities at both interfaces. Owing to the resonant $\chi^{(2)}_{\mathrm{res}}$ contribution, the SHG field enhanced at the top interface destructively interferes with the one generated at the bottom interfaces, which explains the experimentally observed SHG intensity minima. Within this approach, using equation (13) and assuming the resonant $\chi^{(2)}_{\mathrm{res}}$ given by equation (12) we were able to fit the experimental angular spectra of both SHG intensity and magnetic contrast [45]. The frequency dependence over the dispersive SPP spectral range revealed that the maximum value of 33% mSHG contrast remained constant whereas its angular width decreased as the nonlinear SPP resonance became narrower (Γ decreased) and shifted towards the fundamental one. As such, the dominant role of the nonlinear SPP resonance in Kretschmann geometry, which is responsible for the increase of the mSHG magnetic contrast, was identified.

In conclusion, the nonlinear magneto-plasmonics offers a strong enhancement of the magnetization-induced effects as compared to its linear counterpart. In the given spectral range one would expect to reach further enhancement of mSHG contrast by systematically varying the individual thicknesses in this multilayer structure along the lines discussed in [69–76].

4. Acousto-plasmonics

4.1. Linear acousto-plasmonics

In previous sections we have investigated stationary properties of metal-ferromagnet multilayer structures. Femtosecond light pulses were used to achieve high peak intensities of electromagnetic radiation facilitating efficient nonlinear optical frequency conversion. However, irradiation of metallic samples with femtosecond optical pulses is known to trigger the complex dynamics of electronic, acoustic and magnetic

excitations [77–80]. In this section we will discuss transient effects of ultrashort acoustic pulses on SPPs.

Among different mechanisms of acoustic generation the so-called thermo-elastic mechanism is the most common one [81, 82]. Absorption of light leads to fast rise of lattice temperature on a sub-picosecond time scale and the build-up of thermo-elastic stress followed by thermal expansion. This process results in the emission of coherent acoustic pulses with the shape resembling the initial energy deposition profile with a characteristic spatial scale δ_{heat}. The acoustic pulse duration is given by δ_{heat}/c_s, where $c_s = \sqrt{C_2/\rho}$ denotes the longitudinal speed of sound, ρ is material density and C_2 is determined by the elastic tensor and depends on the acoustic propagation direction [83].

The heat deposition depth δ_{heat} is determined not only by the optical skin depth, but also by the diffusion depth of laser-excited hot electrons during the thermalization time with initially cold lattice. This depth is given by $\delta_{\text{hot}} \sim \sqrt{\kappa/g}$, where κ and g denote the thermal conductivity and electron-phonon coupling constant in the material, respectively [84]. In plasmonic metals characterized by relatively high thermal conductivity and weak electron-phonon coupling [85] the heat deposition depth $\delta_{\text{heat}} \simeq \delta_{\text{hot}} \sim 100$ nm largely exceeds the optical skin depth resulting in the generation of relatively long acoustic pulses with the duration of a few tens of picoseconds [86].

For noble metal films of thickness smaller than δ_{heat}, the temperature distribution is spatially homogeneous and the thermo-elastic dynamics can be reduced to breathing motion of the entire film consisting of the alternating expansion and contraction. This behavior was evidenced in femtosecond time-resolved pump-probe experiments in Kretschmann configuration [3, 87, 88].

Hot electron diffusion in ferromagnetic metals appears to be less efficient ($\delta_{\text{hot}} \sim \delta_{\text{skin}} \sim$ 10 nm) and results in the overall heat penetration depth $\delta_{\text{heat}} \sim$ 15–20 nm [89, 90]. This short heat penetration depth in combination with a larger speed of sound enables the generation of large-amplitude ultrashort acoustic pulses in ferromagnetic transition metals like Ni, Co and Fe. However, SPPs do not propagate on ferromagnet surfaces thereby rendering the plasmonic detection schemes extremely challenging. Up to now, there are no acousto-plasmonic investigations on thin ferromagnetic films.

The use of hybrid (noble metal)-ferromagnet bilayer structures on a dielectric substrate allows for the generation of ultrashort acoustic pulses in the ferromagnetic transducer and their plasmonic detection at the (noble metal)/air interface, see figure 9(a).

As the duration of the acoustic pulses is conserved upon the transmission from one elastic medium into another one, acoustic pulses generated in cobalt are spatially compressed by a factor of 1.8 (ratio of sound velocities in cobalt and gold) down to 10 nm upon injection in softer gold [90].

Femtosecond time-resolved plasmonic interferometry [23] measures transient phase shifts of the plasmonic interferogram at the gold–air interface (figure 9(b)) caused by thermal and acoustic effects triggered by the absorption of an intense femtosecond pump pulse in cobalt layer.

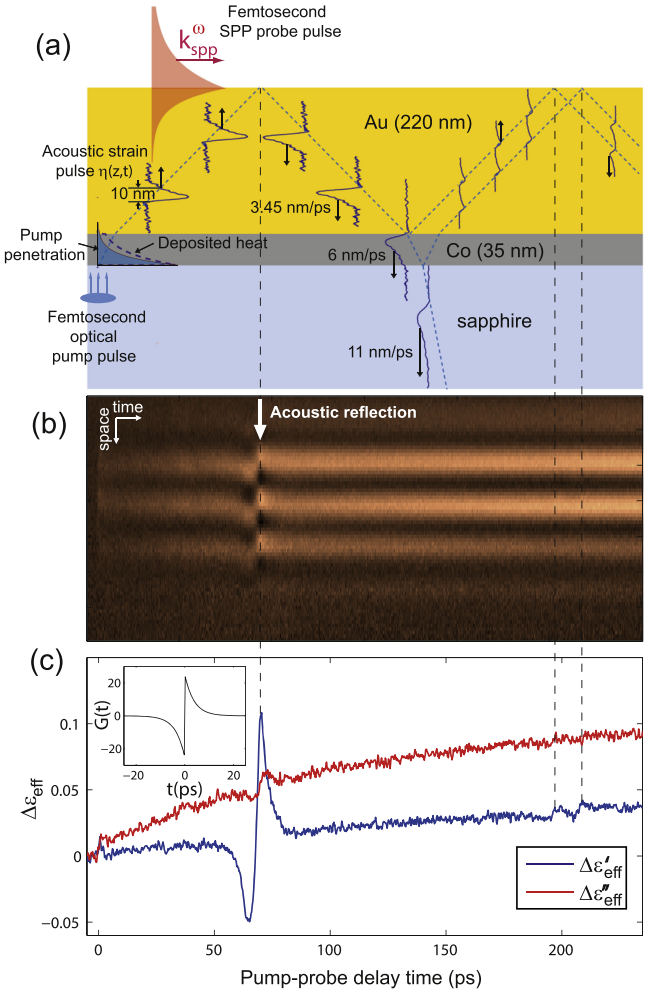

Figure 9. (a) In hybrid acousto-plasmonic structures the thermal expansion of cobalt transducer excited by a femtosecond pump pulse (fluence 7 mJ cm^{-2}) at time zero launches an ultrashort acoustic pulse $\eta(z, t)$ propagating through (111) textured gold layer at the speed of sound $c_s = 3.45$ nm ps^{-1}. After approximately 70 ps, the acoustic reflection from gold–air interface changes the wave vector of a time-delayed ultrashort SPP probe pulse generating the acousto-plasmonic pump-probe interferogram (b) in a tilted slit-groove arrangement. The 10 nm wide acoustic strain pulse in (a) has a duration of 3 ps and is reconstructed from the dynamics of the time-dependent effective dielectric function $\Delta\varepsilon_{\text{eff}}(t)$ in (c). The inset shows the acousto-plasmonic response function $G(t)$. Measurements are performed by time-resolved SPP interferometry [23, 90].

The reconstructed pump-induced modulation $\Delta\varepsilon_{\text{eff}}(t) = \varepsilon_{\text{eff}}(t) - \varepsilon_{\text{Au}}$ in figure 9(c) displays the strong acoustic modulation capturing the reflection of the acoustic pulse $\eta(z, t)$ from the gold–air interface at 70 ps acoustic delay superimposed on a slowly varying thermal background (which will be neglected in the following discussion). The much weaker acousto-plasmonic signals observed at 197 ps and 208 ps are caused by the secondary 10% acoustic reflections from the gold–cobalt and cobalt–sapphire interfaces, respectively, and indicate a good acoustic impedance matching at these interfaces.

The quantitative reconstruction of the acoustic pulse $\eta(z, t)$ propagating in gold relies on the effective medium

approximation. The compressional acoustic pulse in gold $\eta(z, t) = (n_i(z, t) - n_i^0)/n_i^0$ creates a layer of higher ion density $n_i(z, t) > n_i^0$, which moves at the sound velocity $c_s = 3.45\ \mathrm{nm\,ps^{-1}}$ in gold in the (111) direction. Since the stationary charge separation between electrons and ions in a metal occurs only within the Thomas–Fermi radius $r_{TF} \sim 10^{-3}$ nm, the spatial profile of electron (charge) density $n_e(z, t)$ follows the ionic one: $n_e(z, t) = n_i(z, t)$. Evaluated at the probe wavelength of 800 nm, the dielectric function of gold, $\varepsilon_{Au} = \varepsilon' + i\varepsilon'' = -24.8 + 1.5i$, is dominated by the free-carrier contribution with $\varepsilon' \simeq -\omega_p^2/\omega^2 \propto -n_e$. An ultrashort acoustic strain pulse creates a time-dependent spatial profile of the dielectric function $\varepsilon'(z, t) = \varepsilon'[1 + \eta(z, t)]$ inside the metal, which modulates the SPP wave vector $k_{spp}(t) = k_0\sqrt{\varepsilon_{eff}(t)/(1 + \varepsilon_{eff}(t))}$, when the strain pulse arrives within the SPP skin depth $\delta_{skin} = 13$ nm at the gold–air interface:

$$\varepsilon_{eff}(t) = \frac{\varepsilon_{Au}}{\delta_{skin}} \int_0^\infty [1 + \eta(z, t)] \exp(-z/\delta_{skin}) dz. \quad (14)$$

Using the explicit equation for the acoustic reflection at the (free) gold–air interface, $\eta(z, t) = \eta_0(t + z/c_s) - \eta_0(t - z/c_s)$, the integral over space can be converted into the integral over time. The real part of the acoustic modulation

$$\Delta\varepsilon'_{eff}(\tau) = \frac{|\varepsilon_{Au}|}{\tau_{skin}} \int_{-\infty}^{\infty} \eta_0(t) G(\tau - t) dt \quad (15)$$

of the effective dielectric function can be used to reconstruct the acoustic pulse $\eta_0(t)$. Here $\tau_{skin} = \delta_{skin}/c_s = 3.8$ ps denotes the acoustic travel time through the skin depth in gold (at 800 nm wavelength) and the acousto-plasmonic response function $G(t)$, defined as

$$G(t) = \exp(-|t|/\tau_{skin}) \mathrm{sign}(t), \quad (16)$$

is shown in the inset in figure 9(c). Application of the Fourier-based algorithm [91] to $\Delta\varepsilon'_{eff}(\tau)$ allows to accurately reconstruct the acoustic pulse shape $\eta_0(t)$ with duration of 3 ps and spatial extent of 10 nm, as shown in figure 9(a). It is remarkable that plasmonic measurements provide the detailed shape of an acoustic pulse with the spatial dimensions smaller than the skin depth δ_{skin}.

Under certain conditions such shorter-than-skin-depth acoustic pulses can be also measured by simple time-resolved reflectivity measurements at the metal-dielectric interface, as shown for the gold–air interface at 400 nm optical probe wavelength [91].

4.2. Nonlinear acousto-plasmonics

The most striking advantage of the plasmonic interferometry as compared to the conventional pump-probe reflectivity analysis, is that it provides direct measurement of the absolute strain values. Upon increase of the peak pump fluence up to 30 mJ cm^{-2}, the acoustic pulses reach very large amplitude of 1% and also change their shape, see figure 10(a). The acoustic reshaping at high pump fluences becomes more pronounced in thicker gold films, which allowed us to establish its close relation to the acoustic propagation effects in gold [90]. The

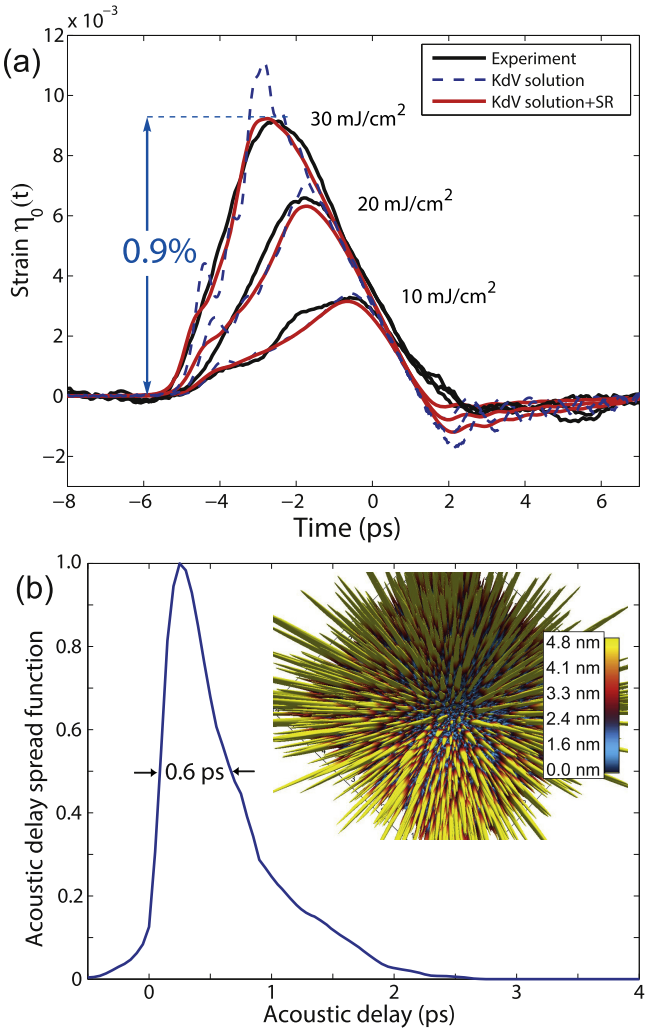

Figure 10. (a) The amplitude of acoustic pulses grows with the pump fluence, reaching nearly 1% whereas their shape changes. These shape changes are reversible and can be quantitatively described by the nonlinear acoustic propagation effects through a 220 nm thin gold layer. (b) Examination of the surface roughness (SR) by an atomic force microscopy (AFM) allows for the measurement of the topography of the gold–air interface. The nano-scale surface roughness (see the 3D-map of $5 \times 5\ \mu m^2$ AFM scan in the inset) introduces substantial spread of the acoustic arrival times at the gold–air interface, quantified by the acoustic delay spread function. Figure (a) adopted with permission from [90].

peak of the acoustic pulse, where the density of gold is higher, propagates through the gold layer at a higher speed of sound leading to the steepening of the acoustic pulse.

The results of the acousto-plasmonic measurements are found to be in an excellent quantitative agreement with the solutions of the nonlinear Korteveg-de Vries (KdV) equation [92]

$$\frac{\partial\eta}{\partial t} + c_s\frac{\partial\eta}{\partial z} + \gamma\frac{\partial^3\eta}{\partial z^3} + \frac{C_3}{2\rho c_s}\eta\frac{\partial\eta}{\partial z} = 0. \quad (17)$$

These dynamics are governed by the interplay between the acoustic broadening due to the phonon dispersion $\omega(q) = c_s q - \gamma q^3$ with $\gamma = 7.41 \times 10^{-18}$ m^3 s^{-1} and self-steepening and reshaping due to the elastic nonlinearity

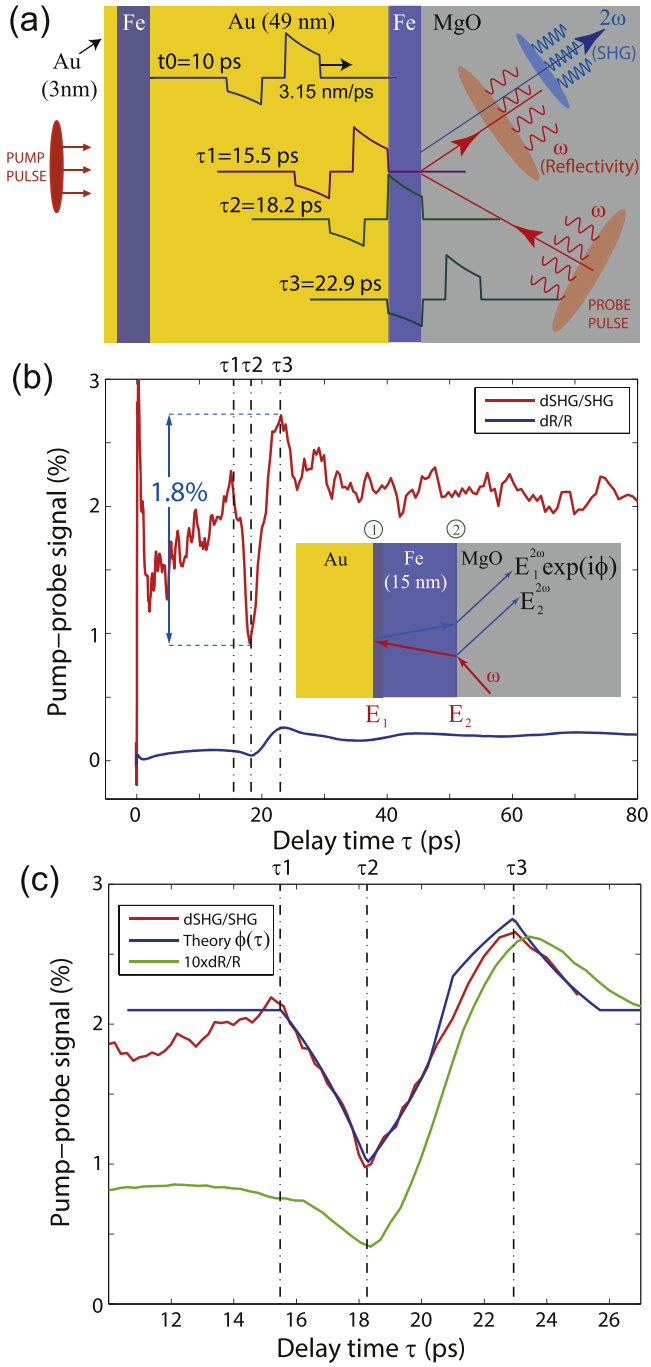

Figure 11. (a) Femtosecond optical pumping of an epitaxial (3 nm) Au/(16 nm)Fe/(49 nm)Au/(15 nm)Fe/MgO multilayer structure leads to the generation of a bipolar acoustic pulse propagating across the sample. (b) When passing through the second Fe layer, the acoustic pulse changes both linear reflectivity and SHG response to the ultrashort probe pulses. The inset shows a possible mechanism of SHG generation via two interfering contributions $E_1^{2\omega}$ and $E_2^{2\omega}$ from Au/Fe and Fe/MgO interfaces. (c) A high-resolution temporal scan shows a remarkable similarity in the dynamics of a strain-induced modulation of the optical phase $\phi(\tau)$ (see text for details).

$C_3 = -2.63 \times 10^{12}$ kg m^{-1} s^{-2}. See [83] for a definition of C_3 and [93, 94] for linear and higher order elastic constants in gold; $\rho = 19.2$ g cm^{-3} is the density of gold. The agreement between the nonlinear theory and the experiment is achieved by setting a single fit parameter, the initial heat penetration depth in cobalt to $\delta_{\text{heat}} = 20$ nm (corresponding to the initial pulse duration $\tau_0 = 3.2$ ps). This value is 50% larger than the optical skin depth in cobalt of 13 nm, indicating the importance of the electronic transport phenomena for establishing the initial distribution of thermal stress driving the thermo-elastic generation.

The quantitative agreement between theory and experiment for samples with different gold thickness demonstrated that nonlinear reshaping was dominated by acoustic nonlinearities in gold, whereas a possible dependence of the initial strain shape in cobalt on pump power played a minor role [90]. The amplitude of the acoustic strain reached peak values $\eta_{\max} \simeq 1\%$, corresponding to a compressional stress $\mathrm{d}p = c_s^2 \rho \eta_{\max} = 2.3$ GPa before acoustic reflection and negative -2.3 GPa tensile stress afterwards. Control measurements at lower pump fluences confirmed that the nonlinear reshaping presented in figure 10(a) was fully reversible. At even higher pump fluences in the range of 50 mJ cm^{-2}, strain pulses with amplitudes reaching 1.5% were obtained. However, under such strong optical pumping consistent with elevating the lattice temperature in cobalt close to its melting point of 1768 K, irreversible degradation of the samples was observed.

Intrinsic damping of longitudinal phonons in gold caused by anharmonic phonon-phonon interactions [95] becomes increasingly important for frequencies exceeding 1 THz. However, in this frequency range and for our experimental geometry, the effect of nano-scale surface roughness entirely masks possible contributions due to phonon attenuation.

In order to illustrate this effect we have studied the topography of the gold–air interface at the position on the sample where acousto-plasmonic measurements were performed, by means of the atomic force microscopy (AFM). The inset in figure 10(b) shows a 3D representation of surface as seen by the acoustic pulses: given the tiny 3.45 nm wavelength of longitudinal acoustic phonons in (111) gold at 1 THz frequency, the nanoscale surface roughness results in the substantial distribution of acoustic arrival times at the gold–air interface. This effect is quantified in the histogram of the acoustic arrival times at the gold–air interface, which we denote as an acoustic delay spread function with a characteristic width of 0.6 ps. Therefore, all possible high-frequency components exceeding 1 THz forming ultrafast acoustic transients on a sub-picosecond time scale (such as, for example, acoustic solitons [83, 92, 96, 97]) are smeared out by the convolution with the response function (compare KdV and KdV+SR curves in figure 10(a)).

The nonlinearity of acoustic propagation can be used to calibrate the conventional pump-probe reflectivity measurements, when the latter are compared with a quantitative experimental technique capable to measure the absolute values of strain amplitudes. Both ultrafast x-ray diffraction [98] and acousto-plasmonic interferometry [90] are reliable techniques to investigate this kind of systems. For example, the comparison of the KdV solutions with the fingerprints of the nonlinear acoustic reshaping observed in femtosecond

pump-probe reflectivity measurements on the same structures [99] provides the values for photo-elastic coefficients $dn/d\eta = 2 \pm 0.7$ and $dk/d\eta = 1 \pm 0.3$ in gold at 400 nm probe wavelength, where $n + ik = 1.47 + 1.95i$ denotes the complex index of refraction. Accurately calibrated time-resolved reflectivity measurements carry the same physical information while offering considerable advantage over more complex quantitative techniques based on SPPs or x-rays.

When thinking in terms of the Kretschmann configuration, the nonlinearity of the acoustic propagation is unlikely to play a role due to the much smaller thickness, which typically does not exceed 50 nm for the entire multilayer structure. In contrast, the entire excitement about the nonlinear magneto-plasmonics is triggered by a much larger effect in the optical nonlinearities as compared to conventional plasmonics. It would be very instructive to learn if SHG intensity can be modulated by ultrashort acoustic pulses as well.

Here we illustrate a novel and poorly understood phenomenon of SHG modulation by acoustic pulses [100–102] with an example of femtosecond pump-probe measurements on a Au/Fe/Au/Fe multilayer structure grown epitaxially on a MgO(001) substrate. This multilayer structure has been designed to study ultrafast transport of spin-polarized hot carriers in gold injected from laser-excited ferromagnetic iron [103].

In this study, we consider the influence of the acoustic pulses generated in the first 16 nm thin iron layer on the SHG output in the second one, see figure 11. The elementary and oversimplified understanding of photo-acoustic generation suggests that femtosecond pump pulses are primarily absorbed in iron which then generates acoustic pulses propagating in both directions. A 3 nm thin layer of gold aiming to protect the upper iron layer from oxidation acts as an acoustic delay line and results in the bi-polar acoustic pulse emitted into the thicker (49 nm) epitaxial Au(001) layer. An approximate pulse shape is shown in figure 11(a) for three distinct time moments τ_1, τ_2 and τ_3 corresponding to the arrival times of the sharp acoustic fronts at the second Fe/Au interface. This schematic helps to understand the effect of acoustic pulses on the linear reflectivity and SHG output from the second iron layer with the thickness $d_{Fe} = 15$ nm, see figure 11(b) and their high-resolution temporal zoom in figure 11(c). A few remarkable observations can be inferred from these measurements. First, the nonlinear acoustically-induced modulation $dI_{2\omega}/I_{2\omega}$ appears to be almost an order of magnitude larger as compared to the linear acoustic modulation $dR(t)/R$. Second, both optical signals are precisely correlated with the arrival times of acoustic fronts at the interfaces.

Interestingly, transient $dI_{2\omega}/I_{2\omega}$ (dSHG/SHG in figure 11) is a continuous function of time. A comparison of the SHG output variations with the linear reflectivity measurements in figure 11(c) clearly shows that the maximum compression (dilution) of the second iron layer correspond to the minimum (maximum) of both SHG intensity and reflectivity modulation. However, the fact that the kinks in the transient variations of the SHG signal are significantly narrower than those in linear reflectivity data demonstrates the extreme sharpness of the fronts of the acoustic pulses.

In centrosymmetric media SHG may arise due to electro-dipole (interface) or magneto-dipole and electro-quadrupole (bulk) contributions. It is commonly believed that the bulk contributions in metals are small as compared to the interface terms [50, 52, 104]. On the other hand, inversion symmetry in the bulk can be broken, for example, by a gradient of strain resulting in the allowed volumetric electro-dipole contribution. Whereas static strain gradients emerge from the growth on a lattice-mismatched substrate, dynamic strain gradients can be induced by ultrashort acoustic pulses. Another possible mechanism relies upon transient acoustic modulation of the surface properties of Fe, including the susceptibility tensor $\chi^{(2)}$. In any case, the total SHG output is produced by an interference of multiple SHG sources, whereas the interference conditions are strongly affected by the propagating acoustic pulses.

Despite these ambiguities, the shape of acoustically-induced SHG output modulation can be described within a simple model which considers an interference of the two surface SHG contributions $E_1^{2\omega}\exp(i\phi_0)$ and $E_2^{2\omega}$ generated at the Au/Fe and Fe/MgO interfaces. Here ϕ_0 denotes the phase difference between these two interfering terms suggesting that the total SHG intensity is proportional to $I_{2\omega} \propto |E_1^{2\omega}\exp(i\phi_0) + E_2^{2\omega}|^2$. An acoustic pulse $\eta(z, \tau)$ propagating through the iron layer modulates this optical phase $\phi(\tau) = \phi_0 + \Delta\phi(\tau)$ according to

$$\Delta\phi(\tau) \propto \frac{2\pi}{\lambda}\int_0^{d_{Fe}} \eta(z, \tau)dz, \tag{18}$$

where the integration is performed over the entire Fe layer. As such, we obtain $dI_{2\omega} = -(2E_1^{2\omega}E_2^{2\omega}\sin\phi_0)\Delta\phi(\tau)$. Using the acoustic pulse shape shown in figure 11(a) and equation (18) we have calculated transient phase variations $\Delta\phi(\tau)$.

With an appropriate scaling factor (which depends on the photo-elastic coefficients of iron at fundamental and/or SHG wavelengths) and vertical offset (thermal background), this simulated phase shift demonstrates surprising similarity to the experimental SHG signal in figure 11(c). We note, however, that at present the underlying origin of this phase modulation remains unclear. Due to the nonlinear character of the discussed interference, this phase modulation is acquired by either the driving fundamental fields E_1, E_2 or the emitted SHG field at the double frequency 2ω.

From a practical perspective, these preliminary experimental observations and theoretical modeling hold high potential in application to the nonlinear plasmonics and magneto-plasmonics. They can serve as a first step to test the effective interface approximation for complex multilayer structures, where a simple interference model can be generalized to include strain-induced modification of bulk SHG terms dominating in semiconductor and dielectic media [100, 102].

A more general phenomenological description using a single time-dependent nonlinear effective susceptibility $\chi_{eff}^{(2)}(t)$ for the upper interface in figure 7(b) would be also useful to understand the physical limits of ultrafast acoustic modulation in the nonlinear magneto-plasmonic switch sketched in figure 1.

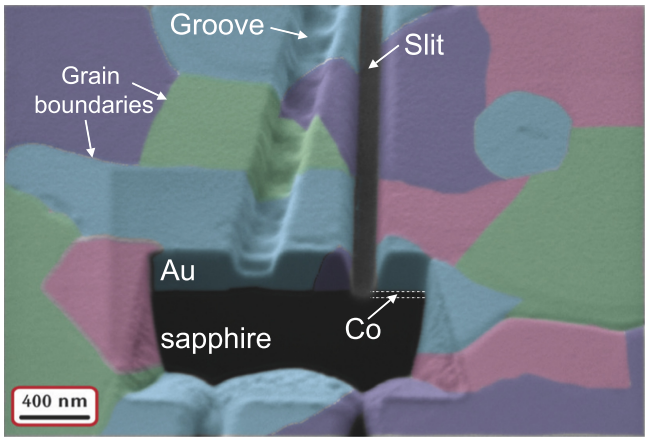

Figure 12. All investigated gold films grown by magnetron sputtering at 250 °C displayed (111) texture and a large grain size of the order of 1 μm. Small changes in the SEM images from secondary electrons were color-coded to show different grains.

5. Fabrication and characterization of multilayer structures

The quality of the samples determines the effects which can be experimentally observed. For instance, for the plasmonic experiments, the key optimization of the samples consists in the minimization of the sample roughness [105]. In stark contrast, ultrafast acoustics turns out to be much more demanding to the sample quality with many parameters drastically influencing the observed signal amplitudes and shapes of the transients. Those parameters include the surface and interface roughness, single- or polycrystallinity of the samples, grain sizes and grain size distribution as well as the texture of the grains. For the latter, due to the large elastic anisotropy of crystalline solids, the acoustic propagation time in grains with different orientation would typically differ by 10% around the average value: The commonly used value of 3200 m s^{-1} for polycrystalline gold differs from 3450 m s^{-1} for (111) and 3150 m s^{-1} for (100) crystallographic directions in gold single crystals.

For the experiments on ultrafast acoustics discussed in this review, the most appropriate substrates are Al_2O_3(0001). Due to their single crystal nature, they assure excellent optical transparency in the relevant frequency range and offer good acoustic impedance matching to cobalt. The latter is a good transducer for ultrafast acoustics because of its high speed of sound and high melting temperature. Since the details of the layer stack are already defined for the efficient magneto-acousto-plasmonics, the remaining optimization of the sample quality (large grain sizes of Au in the range of 1 μm and small surface roughness) is mainly related to the adjustment of the growth parameters of the Co layer and Au films, with the target to improve homogeneity of the respective materials.

One of the key parameters determining the crystalline structure of Co when grown on Al_2O_3(0001) is the deposition temperature. This temperature should be chosen to obtain strong hcp (0001) texture of Co thin films which should promote the growth of the (111) textured Au layer. We note that considering the lattice symmetry and the lattice parameters, it is possible to grow (111) textured Au layer on either hcp (0001) Co or on fcc (111) Co. A rather large lattice mismatch of about 14% between fcc Au(111) and hcp Co(0001) is relieved by formation of misfit dislocations [106], which assures the emergence of laterally extended grains of (111) textured Au on top of the Co film. Aiming for the sample with large Au(111) grains, the deposition of Co at higher temperatures is usually required [107]. For instance, if Co thin films are deposited on Al_2O_3(0001) at temperatures below 150 °C, the fcc (111) textured Co with small Co grains of $<$50 nm is prepared [107]. At temperatures of 250 °C and above, clean hcp texture of Co grains is typically realized independent of the deposition technique; see, e.g. Yabuhara *et al* [107] for the growth of Co/Al_2O_3 using molecular beam epitaxy technique and Brandenburg *et al* [108] using pulsed laser deposition. At this temperature Co films with the thickness of up to 80 nm grow hcp textured with a full epitaxial relation as follows [108]: Co(0001)$\langle$10–10$\rangle$ || Al_2O_3(0001)[11–20]. Although films grown at higher temperatures typically possess larger grain sizes, it is found that the surface roughness of Co thin films drastically increases when the deposition temperature exceeds 250 °C [107]. Therefore, the deposition temperature of 250 °C is chosen as a compromise to have relatively large grain sizes in Co films and assure small surface roughness for the growth of Au layer. Onto the hcp (0001) textured Co film, a Au layer is then deposited. The deposition temperature should be chosen to avoid intermixing at the interface between Co and Au. Accordingly to [109, 110], annealing in H_2/N_2 atmosphere at temperatures up to 300 °C allows to avoid alloying. However, vacuum annealing of Co/Au multilayers up to 250 °C leads to the partial loss of the structural coherence which might be indicative for the Co–Au mixture formation [111]. Based on these considerations, the appropriate temperature window for the growth of both Co and Au layers is between 200 °C and 250 °C.

The deposition of Co and Au thin films is carried out at 250 °C using dc-magnetron sputtering in a high vacuum chamber with a base pressure of 10^{-7} mbar. Double-side epipolished 500 μm thick Al_2O_3(0001) single crystals (Crystec GmbH) with lateral dimensions of 10×10 mm^2 were used as a substrate. The tilt of the *c*-axis of the Al_2O_3(0001) was less than 0.3°. The substrates were fixed to the sample holder using metal clamps assuring good thermal contact. Before the deposition, the substrates were outgassed for 30 min at 250 °C. Ar was used as a sputter gas (Ar pressure is 3.5×10^{-3} mbar). The deposition rate of Co and Au was set to 0.2 Å s^{-1} and 2 Å s^{-1}, respectively. The thickness of Co layer was varied between 2 and 35 nm. The thickness of Au film was chosen between 120 and 780 nm.

The structural analysis of the samples with Co(2 nm; 4 nm; 6 nm)/Au(200 nm) has been performed by x-ray diffraction (XRD) in Bragg-Brentano geometry using Cu K_α irradiation (wavelength: 1.54 Å) on a laboratory diffractometer (XRD 7, Seifert-FPM). Due to the small thickness, the diffraction peaks of Co are not resolved. Independent of the thickness of Co, clear diffraction peaks at

38.36° and 81.92° are observed characteristic of (111) textured Au films. No other peaks are observed.

Although the films are strongly (111) textured, the in-plane orientation of the Au crystallites is random, as can be seen when analyzing the SEM image (figure 12). Different in-plane orientation of the crystallites is shown using false colors. The size of an individual crystallite is in the range of few hundreds of nanometers. Furthermore, the cross-section of the film was studied by cutting it using focused-ion beam etching. We conclude that each grain is uniform in thickness due to the excellent homogeneity in the SEM contrast. This finding has a strong implication for the analysis of the propagation of acoustic pulses in the film: as the gold film is (111) textured, the propagation velocity of an acoustic pulse along the film thickness can be taken as constant and equal to the 3450 m s^{-1}, the characteristic value for the a single crystal with (111) orientation.

6. Discussion and future research

In this study we did not discuss any investigations related to the ultrafast magnetization dynamics [112]. The phenomenon of ultrafast laser-induced demagnetization, either by the direct optical excitation [77] or mediated by the ultrafast transport of non-equilibrium hot electrons across the (noble metal)-ferromagnet interface [79, 80, 103, 113, 114], results in the abrupt decrease in the length of magnetization vector. This phenomenon occurs on a sub-picosecond time scale and can even result in ultrafast magnetization reversal in ferrimagnets [115, 116].

Another option of the laser-induced magnetization control consists in changing the direction of magnetization as evidenced by the excitation of the ferromagnetic resonance (FMR) precession. FMR precession [78, 117, 118] as well as excitation of spatially inhomogeneous (magnon) precessional modes in ferromagnetic thin films [78, 80] originate from the ultrafast thermally-induced changes in the magneto-crystalline anisotropy.

Very recently, it became typical to induce FMR precession via magneto-elastic interactions in ferromagnets, when excited by picosecond acoustic strain pulses [119–121]. So far the acoustically induced FMR precession in thin ferromagnetic films was observed only when the symmetry was broken by the non-zero out-of-plane component of the external magnetic field [119–121]. In the analogous experiments with ultrafast surface acoustic waves (SAW, excited by fs-laser pulses in transient grating geometry [122]), the most efficient excitation of FMR precession was achieved by tilting the external magnetic field with respect to the SAW wave vector [123, 124]. Further, a laser excitation of a coupled magneto-elastic mode with an extreme lifetime of more than 25 ns and strongly nonlinear behavior was demonstrated in ferromagnetic dielectric $FeBO_3$ [125].

Purely acoustic magnetization switching was predicted theoretically for single-crystal thin film of magnetostrictive metal Terfenol-D excited with picosecond acoustic pulses [126] or semiconductor (Ga,Mn)(As,P) driven by quasi-monochromatic SAW transients [127]. Experimentally, acoustic magnetization switching has only been demonstrated in ferromagnetic nanoparticles on the nanosecond time scale [128]. From all these observations we conclude that in the nonlinear magneto-plasmonic switch sketched in figure 1, notably with an in-plane magnetic field applied, the magneto-acoustic effects are unlikely to play a major role.

The substantial modulation of the nonlinear optical properties of 1.8% can be further enhanced by functionalizing the structure with a monolayer of semiconductor QDs. QDs are particularly promising for nonlinear acousto-magneto-plasmonics as they feature configurable 'atom-like' optical excitation spectrum because they offer the ability of engineering of the electron and hole wave functions via the QD size R_{QD}. Nonlinear initialization and readout of singly-charged QDs can be harvested for ultrafast quantum optical functionality [129]. It is known that a linear as well as a nonlinear response in these systems, typically analyzed in the dipole approximation which exploits the approximation $R_{QD} \ll \lambda$, is intimately linked to the details of the spin configuration of the few-electron states as well as the crystal structure and the geometry of the nano-emitter [130, 131]. Application of controlled acoustic transients with considerable enhancement in the elastic field gradients on the length scales comparable to R_{QD} would thus allow for controlled studies of the response of the quantum system beyond the dipole approximation [132]. In other words, if the acoustic pulse can significantly perturb the electron eigenstates in the QD, new fascinating electromagnetic effects of substantially non-local nature can be expected. This nonlinear coupled regime has not been well explored so far and might provide new physical insights and therefore inspire novel photonic applications.

As a parting example we speculate that by subjecting colloidal QDs [133] to intense acoustic transients such as those reviewed here, one might be able to drive structural phase transition [134] in these nano crystal on ultrafast timescales. As a result, one would be able to directly switch and control the brightness of the quantum emitter [130] on femtosecond time scales.

Beyond the SHG response, higher nonlinearities such as third-order susceptibility-driven magnetic third harmonic generation (mTHG) can be exploited to great effect. Indeed, mTHG allows to evaluate bulk (as compared to surface mSHG) nonlinearities and also draw analogies to the giant magnetoresistance properties in ferromagnetic nanostructures [135]. In our case, for the THG frequency to fall in the visible spectral range, one would need to apply pump excitation with a wavelength in the near-infrared spectral range [136, 137]. Employing the telecom wavelengths ($\lambda = 1.3$ or 1.5 μm) would allow to simultaneously detect mSHG and mTHG in the visible spectral range, while exploiting mature technology of ultrabroadband femtosecond fiber lasers [138]. Moreover, in this case SPP excitation at the first and the second harmonic frequencies will occur at nearly the same angle and as a result would lead to a more favorable phase-matching condition between the SPPs, $k_{spp}^{2\omega} \simeq 2k_{spp}^{\omega}$. Moving to even longer wavelengths and using intense pulses of THz radiation as an

effective stimulus may enable efficient high-order harmonic generation with SPPs.

To summarize, in this review we have discussed some recent developments in the field of the nonlinear acousto-magneto-plasmonics, which are necessary for understanding of the fundamental interactions and the associated time and length scales of the nonlinear plasmonic switch sketched in figure 1. The extension of the concepts presented here to hybrid plasmonic structures as well as to semiconductor nanostructures, together with shifting the experimental focus to lower photon energies and higher-order optical nonlinearities hold high potential for future research.

Acknowledgments

Authors thank A Alekhin (IMMM CNRS 6283) for performing the nonlinear SHG-measurements shown in figure 11 and T Thomay (SUNY at Buffalo) for focussed ion beam milling of the plasmonic microinterferometers and taking a false-color SEM image of Au/Co/sapphire structure in figure 12. They also acknowledge stimulating discussions with U Woggon, A. Leitenstorfer, A Kirilyuk, Th Rasing, T V Murzina, R Bratschitsch, R Tobey, A Garcia-Martin, V S Vlasov, A M Lomonosov, V Juvé P Ruello, V E Gusev, I Radu, U Bovensiepen, T Kampfrath, M Bargheer, P Gaal and M Wolf.

Funding from *Nouvelle équipe, nouvelle thématique* 'Ultrafast acoustics in hybrid magnetic nanostructures' and *Stratégie internationale* 'NNN-Telecom' de la Région Pays de La Loire, DFG (TE770/1), ANR-DFG 'PPMI-NANO' (ANR-15-CE24-0032 & DFG SE2443/2), ANR 'UltramoX' (ANR-14-CE26-0008), U.S. DOE Grant no. DE-FG02-00ER15087, U.S. NSF Grant no. CHE-1111557, the European Research Council (FP7/2007-2013)/ERC grant agreement no. 306277 and *Alexander von Humboldt Stiftung* is highly appreciated.

References

[1] Fedutik Y, Temnov V V, Schöps O, Woggon U and Artemyev M V 2007 Exciton–plasmon–photon conversion in plasmonic nanostructures *Phys. Rev. Lett.* **99** 136802

[2] Ueda A, Tayagaki T and Kanemitsu Y 2008 Energy transfer from semiconductor nanocrystal monolayers to metals surfaces revealed by time-resolved photoluminescence spectroscopy *Appl. Phys. Lett.* **92** 133118

[3] van Exter M and Lagendijk A 1988 Ultrashort surface-plasmon and phonon dynamics *Phys. Rev. Lett.* **60** 49–52

[4] MacDonald K F, Samson Z L, Stockman M I and Zheludev N I 2008 Ultrafast active plasmonics *Nat. Photon.* **3** 55–8

[5] Kauranen M and Zayats A V 2012 Nonlinear plasmonics *Nat. Photon.* **6** 737–48

[6] Mukherjee S, Libisch F, Large N, Neumann O, Brown L V, Cheng J, Lassiter J B, Carter E A, Nordlander P and Halas N J 2013 Hot electrons do the impossible: plasmon-induced dissociation of H_2 on Au *Nano Lett.* **13** 240–7

[7] Temnov V V 2012 Ultrafast acousto-magneto-plasmonics *Nat. Photon.* **6** 728–36

[8] Temnov V V 2015 Nonlinear acousto-magneto-plasmonics for ultrafast switching *SPIE Newsroom* (doi:10.1117/2.1201508.006039)

[9] Barnes W L, Dereux A and Ebbesen T W 2003 Surface plasmon subwavelength optics *Nature* **424** 824–30

[10] Schmidt M K, Mackowski S and Aizpurua J 2012 Control of single emitter radiation by polarization- and position-dependent activation of dark antenna modes *Opt. Lett.* **37** 1017

[11] Anger P, Bharadwaj P and Novotny L 2006 Enhancement and quenching of single-molecule fluorescence *Phys. Rev. Lett.* **96** 113002

[12] Pelton M, Aizpurua J and Bryant G 2008 Metal-nanoparticle plasmonics *Laser Photon. Rev.* **2** 136–59

[13] Wang K and Mittleman D M 2006 Dispersion of surface plasmon polaritons on metal wires in the terahertz frequency range *Phys. Rev. Lett.* **96** 157401

[14] Ditlbacher H, Hohenau A, Wagner D, Kreibig U, Rogers M, Hofer F, Aussenegg F R and Krenn J R 2005 Silver nanowires as surface plasmon resonators *Phys. Rev. Lett.* **95** 257403

[15] Allione M, Temnov V V, Fedutik Y, Woggon U and Artemyev M V 2008 Surface plasmon mediated interference phenomena in low-q silver nanowire cavities *Nano. Lett.* **8** 31

[16] Li Q and Qiu M 2013 Plasmonic wave propagation in silver nanowires: guiding modes or not? *Opt. Express* **21** 8587–95

[17] Guo X, Ma Y, Wang Y and Tong L 2013 Nanowire plasmonic waveguides, circuits and devices *Las. Photon. Rev.* **7** 855–81

[18] Kretschmann E and Raether H 1968 Radiative decay of non radiative surface plasmons excited by light *Z. Naturforsch.* **23a** 2135–6

[19] Burke J J, Stegeman G I and Tamir T 1986 Surface-polariton-like waves guided by thin, lossy metal films *Phys. Rev.* B **33** 5186

[20] Weber W H and Ford G W 1981 Optical electric-field enhancement at a metal surface arising from surface-plasmon excitation *Opt. Lett.* **6** 122

[21] Khurgin J B 2015 How to deal with the loss in plasmonics and metamaterials *Nat. Nanotechnol.* **10** 2–6

[22] Nagpal P, Lindquist N C, Oh S H and Norris D J 2009 Ultrasmooth patterned metals for plasmonics and metamaterials *Science* **325** 594–7

[23] Temnov V V, Nelson K, Armelles G, Cebollada A, Thomay T, Leitenstorfer A and Bratschitsch R 2009 Femtosecond surface plasmon interferometry *Opt. Express* **17** 8423–32

[24] Zayats A V, Smolyaninov I I and Maradudin A A 2005 Nano-optics of surface plasmon polaritons *Phys. Rep.* **408** 131–314

[25] Gay G, Alloschery O, Viaris de Lesegno B, O'Dwyer C, Weiner J and Lezec H J 2006 The response of nanostructured surfaces in the near field *Nat. Phys.* **2** 262

[26] Temnov V V, Woggon U, Dintinger J, Devaux E and Ebbesen T W 2007 Surface plasmon interferometry: measuring group velocity of surface plasmons *Opt. Lett.* **32** 1235

[27] Pacifici D, Lezec H J and Atwater H A 2007 All-optical modulation by plasmonic excitation of CdSe quantum dots *Nat. Photon.* **1** 402–6

[28] Armelles G, Cebollada A, Garcia-Martin A and Gonzalez M U 2013 Magnetoplasmonics: combining magnetic and plasmonic functionalities *Adv. Opt. Mater.* **1** 10–35

[29] Ctistis G, Papaioannou E, Patoka P, Gutek J, Fumagalli P and Giersig M 2009 Optical and magnetic properties of

hexagonal arrays of subwavelength holes in optically thin cobalt films *Nano Lett.* **9** 1–6
[30] Demidenko Y, Makarov D, Schmidt O G and Lozovski V 2011 Surface plasmon-induced enhancement of the magneto-optical kerr effect in magnetoplasmonic heterostructures *J. Opt. Soc. Am.* B **28** 2115
[31] Bonanni V, Bonetti S, Pakizeh T, Pirzadeh Z, Chen J, Nogues J, Vavassori P, Hillenbrand R, Åkerman J and Dmitriev A 2011 Designer magnetoplasmonics with nickel nanoferromagnets *Nano Lett.* **11** 5333–8
[32] Belotelov V I *et al* 2013 Plasmon-mediated magneto-optical transparency *Nat. Commun.* **4** 2128
[33] Crassee I, Orlita M, Potemski M, Walter A L, Ostler M, Seyller T, Gaponenko I, Chen J and Kuzmenko A B 2012 Intrinsic terahertz plasmons and magnetoplasmons in large scale monolayer graphene *Nano Lett.* **12** 2470–4
[34] Maccaferri N *et al* 2013 Tuning the magneto-optical response of nanosize ferromagnetic Ni disks using the phase of localized plasmons *Phys. Rev. Lett.* **111** 167401
[35] Shcherbakov M R, Vabishchevich P P, Frolov A Y, Dolgova T V and Fedyanin A A 2014 Femtosecond intrapulse evolution of the magneto-optic kerr effect in magnetoplasmonic crystals *Phys. Rev.* B **90** 201405(R)
[36] Autore M, Engelkamp H, D'Apuzzo F, Di Gaspare A, Di Pietro P, Lo Vecchio I, Brahlek M, Koirala N, Oh S and Lupi S 2012 Observation of magnetoplasmons in Bi_2Se_3 topological insulator *ACS Photon.* **2** 1231–5
[37] Maccaferri N, Gregorczyk K E, de Oliveira T V A G, Kataja M, van Dijken S, Pirzadeh Z, Dmitriev A, Åkerman J, Knez M and Vavassori P 2015 Ultrasensitive and label-free molecular-level detection enabled by light phase control in magnetoplasmonic nanoantennas *Nat. Commun.* **6** 6150
[38] Maccaferri N, Bergamini L, Pancaldi M, Schmidt M K, Kataja M, van Dijken S, Zabala N, Aizpurua J and Vavassori P 2016 Anisotropic nanoantenna-based magnetoplasmonic crystals for highly enhanced and tunable magneto-optical activity *Nano Lett.* **16** 2533–42
[39] Kataja M, Pourjamal S, Maccaferri N, Vavassori P, Hakala T K, Huttunen M J, Törmä P and van Dijken S 2016 Hybrid plasmonic lattices with tunable magneto-optical activity *Opt. Express* **4** 3652–62
[40] Maksimov I S 2015 Magneto-plasmonics and resonant interaction of light with dynamic magnetisation in metallic and all-magneto-dielectric nanostructures *Nanomaterials* **5** 577–613
[41] Maccaferri N, Inchausti X, Garcia-Martin A, Cuevas J C, Tripathy D, Adeyeye A O and Vavassori P 2015 Resonant enhancement of magneto-optical activity induced by surface plasmon polariton modes coupling in 2D magnetoplasmonic crystals *ACS Photon.* **2** 1769–79
[42] Rollinger M, Thielen P, Melander E, Ostman E, Kapaklis V, Obry B, Cinchetti M, Garcia-Martin A, Aeschlimann M and Papaioannou E T 2016 Light localization and magneto-optic enhancement in Ni antidot arrays *Nano Lett.* **16** 2432–8
[43] Gonzalez-Diaz J B, Garcia-Martin A, Armelles G, Garcia-Martin J-M, Clavero C, Cebollada A, Lukaszew R A, Skuza J R, Kumah D P and Clarke R 2007 Surface magnetoplasmon nonreciprocity effects in noble-metal/ferromagnetic heterostructures *Phys. Rev.* B **76** 153402
[44] Temnov V V, Armelles G, Woggon U, Guzatov D, Cebollada A, Garcia-Martin A, Garcia-Martin J M, Thomay T, Leitenstorfer A and Bratschitsch R 2010 Active magneto-plasmonics in hybrid metal-ferromagnet structures *Nat. Photon.* **4** 107–10
[45] Razdolski I, Makarov D, Schmidt O G, Kirilyuk A, Rasing T and Temnov V V Nonlinear surface magnetoplasmonics in Kretschmann multilayers *ACS Photon.* **3** 179–83
[46] Torrado J F, Gonzalez-Diaz J B, Garcia-Martin A and Armelles G 2013 Unraveling the relationship between electromagnetic field intensity and the magnetic modulation of the wave vector of coupled surface plasmon polaritons *New J. Phys.* **15** 075025
[47] Belotelov V I, Bykov D A, Doskolovich L L, Kalish A N and Zvezdin A K 2009 Extraordinary transmission and giant magneto-optical transverse kerr effect in plasmonic nanostructured films *J. Opt. Soc. Am.* B **26** 1594–8
[48] Foley J J IV, Harutyunyan H, Rosenmann D, Divan R, Wiederrecht G P and Gray S K 2015 When are surface plasmon polaritons excited in the Kretschmann–Raether configuration? *Sci. Rep.* **5** 9929
[49] Zheng W, Liu X, Hanbicki A T, Jonker B T and Lüpke G 2015 Nonlinear magneto-plasmonics *Opt. Mater. Express* **5** 2597–607
[50] Raschke M B, Berweger S and Atkin J M 2013 Ultrafast and nonlinear plasmon dynamics *Plasmonics: Theory and Applications* ed T V Shahbazyan and M I Stockman (Berlin: Springer) pp 237–81
[51] Simon H J, Mitchell D E and Watson J G 1974 Optical second-harmonic generation with surface plasmons in silver films *Phys. Rev. Lett.* **33** 1531–4
[52] Heinz T F 1991 *Second-Order Nonlinear Optical Effects at Surfaces and Interfaces* (Amsterdam: Elsevier) pp 353–416 ch 5
[53] de Martini F and Shen Y R 1976 Nonlinear excitation of surface polaritons *Phys. Rev. Lett.* **36** 216–9
[54] Palomba S and Novotny L 2008 Nonlinear excitation of surface plasmon polaritons by four-wave mixing *Phys. Rev. Lett.* **101** 056802
[55] Pan R-P, Wei H D and Shen Y R 1989 Optical second-harmonic generation from magnetized surfaces *Phys. Rev.* B **39** 1229–34
[56] Krutyanskiy V L, Kolmychek I A, Ganshina E A, Murzina T V, Evans P, Pollard R, Stashkevich A A, Wurtz G A and Zayats A V 2013 Plasmonic enhancement of nonlinear magneto-optical response in nickel nanorod metamaterials *Phys. Rev.* B **87** 035116
[57] Razdolski I, Gheorghe D G, Melander E, Hjörvarsson B, Patoka P, Kimel A V, Kirilyuk A, Papaioannou E T and Rasing T 2013 Nonlocal nonlinear magneto-optical response of a magnetoplasmonic crystal *Phys. Rev.* B **88** 075436
[58] Krutyanskiy V L, Chekhov A L, Ketsko V A, Stognij A I and Murzina T V 2015 Giant nonlinear magneto-optical response of magnetoplasmonic crystals *Phys. Rev.* B **91** 121411(R)
[59] Murzina T V, Misuryaev T V, Kravets A F, Guedde J, Schuhmacher D, Marowsky G, Nikulin A A and Aktsipetrov O A 2001 Nonlinear magneto-optical kerr effect and plasmon-assisted SHG in magnetic nanomaterials exhibiting giant magnetoresistance *Surf. Sci.* **482–485** 1101–6
[60] Aktsipetrov O A, Murzina T V, Kim E M, Kapra R V, Fedyanin A A, Inoue M, Kravets A F, Kuznetsova S V, Ivanchenko M V and Lifshits V G 2005 Magnetization-induced second- and third-harmonic generation in magnetic thin films and nanoparticles *J. Opt. Soc. Am.* B **22** 138–47
[61] Kolmychek I A, Murzina T V, Fourier S, Wouters J, Valev V K, Verbiest T and Aktsipetrov O A 2009 Second harmonic generation in core (shell) γ-Fe_2O_3 (Au) nanoparticles *Sol. State Phenom.* **152-153** 508–11
[62] Valev V K *et al* 2011 Plasmons reveal the direction of magnetization in nickel nanostructures *ACS Nano* **5** 91–6
[63] Zheng W, Hanbicki A, Jonker B T and Lüpke G 2014 Control of magnetic contrast with nonlinear magneto-plasmonics *Sci. Rep.* **4** 1–5
[64] Grosse N B, Heckmann J and Woggon U 2012 Nonlinear plasmon-photon interaction resolved by k-space spectroscopy *Phys. Rev. Lett.* **108** 136802

[65] Knight M W, Liu L, Yang X, Brown L, Mukherjee S, King N S, Everitt H O, Nordlander P and Halas N J 2012 Aluminum plasmonic nanoantennas *Nano Lett.* **12** 6000–4

[66] Naik G V, Shalaev V M and Boltasseva A 2013 Alternative plasmonic materials: beyond gold and silver *Adv. Mater.* **25** 3264–94

[67] Knight M W, King N S, Liu L, Everitt H O, Nordlander P and Halas N J 2014 Alumimun for plasmonics *ACS Nano* **8** 834–40

[68] Gong C and Leite M 2014 Noble metal alloys for plasmonics *ACS Photon.* **3** 507–13

[69] Heckmann J, Kleemann M-E, Grosse N B and Woggon U 2013 The dual annihilation of a surface plasmon and a photon by virtue of a three-wave mixing interaction *Opt. Express* **21** 28856–61

[70] Pavlov V V, Tessier G, Malouin C, Georges P, Brun A, Renard D, Meyer P, Ferre J and Beauvillain P 1999 Observation of magneto-optical second-harmonic generation with surface plasmon excitation in ultrathin Au/Co/Au films *Appl. Phys. Lett.* **75** 190–2

[71] Rasing T 1994 Studies of buried interfaces by optical second-harmonic generation *Appl. Phys.* A **59** 531–6

[72] Wierenga H A, Prins M W J, Abraham D L and Rasing T 1994 Magnetization-induced optical second-harmonic generation: a probe for interface magnetism *Phys. Rev.* B **50** 1282–6

[73] Jin Q Y, Regensburger H, Vollmer R and Kirschner J 1997 Periodic oscillations of the surface magnetization during the growth of Co films on Cu(001) *Phys. Rev. Lett.* **80** 4056–9

[74] Sato K, Kodama A, Miyamoto M, Takanashi K, Fujimori H and Rasing T 2000 Nonlinear magneto-optical effect in Fe/Au superlattices modulated by noninteger atomic layers *J. Appl. Phys.* **87** 6785–7

[75] Vollmer R, Regensburger H, Wu Y Z and Kirschner J 2001 Magnetization induced second harmonic generation from ultrathin metallic multilayers *Phys. Status Solidi* (a) **188** 1513–24

[76] Jähnke V, Güdde J and Matthias E 2001 Growth and magnetic ordering of Ni and Co films on rh(0 0 1) investigated with second-harmonic generation *J. Magn. Magn. Mater.* **232** 27–35

[77] Beaurepaire E, Merle J C, Daunois A and Bigot J-Y 1996 Ultrafast spin dynamics in ferromagnetic nickel *Phys. Rev. Lett.* **76** 4250–3

[78] van Kampen M, Jozsa C, Kohlhepp J T, LeClair P, Lagae L, de Longe W J M and Koopmans B 2002 All-optical probing of coherent spin waves *Phys. Rev. Lett.* **88** 227201

[79] Eschenlohr A, Battiato M, Maldonado P, Pontius N, Kachel T, Holldack K, Mitzner R, Fohlisch A, Oppeneer P M and Stamm C 2013 Ultrafast spin transport as key to femtosecond demagnetization *Nat. Mater.* **12** 332–6

[80] Shalagatskyi V, Kovalenko O, Shumylo V, Pezeril T, Mounier D, Gusev V E, Makarov D and Temnov V V 2015 Ultrafast electron-phonon-magnon interactions at noble metal-ferromagnet interfaces arXiv:1511.09060

[81] Thomsen C, Grahn H T, Maris H J and Tauc J 1986 Surface generation and detection of phonons by picosecond light pulses *Phys. Rev.* B **34** 4129–38

[82] Matsuda O, Larciprete M C, Voti R L and Wright O B 2015 Fundamentals of picosecond laser ultrasonics *Ultrasonics* **56** 3–20

[83] Hao H Y and Maris H J 2001 Experiments with acoustic solitons in crystalline solids *Phys. Rev.* B **64** 064302

[84] Tas G and Maris H J 1994 Electron diffusion in metals studied by picosecond ultrasonics *Phys. Rev.* B **49** 15046

[85] Del Fatti N, Voisin C, Achermann M, Tzortzakis S, Christofilos D and Vallée F 2000 Nonequilibrium electron dynamics in noble metals *Phys. Rev.* B **61** 16956–66

[86] Gusev V E and Wright O B 1998 Ultrafast nonequilibrium dynamics of electrons in metals *Phys. Rev.* B **57** 2878

[87] Wang J, Wu J and Guo C 2007 Resolving dynamics of acoustic phonons by surface plasmons *Opt. Lett.* **32** 719–21

[88] Wang J and Guo C 2007 Effect of electron heating on femtosecond laser-induced coherent acoustic phonons in noble metals *Phys. Rev.* B **75** 184304

[89] Saito T, Matsuda O and Wright O B 2003 Picosecond acoustic phonon pulse generation in nickel and chromium *Phys. Rev.* B **67** 205421

[90] Temnov V V, Klieber C, Nelson K A, Thomay T, Knittel V, Leitenstorfer A, Makarov D, Albrecht M and Bratschitsch R 2013 Femtosecond nonlinear ultrasonics in gold probed with ultrashort surface plasmons *Nat. Commun.* **4** 1468

[91] Manke1 K J, Maznev A A, Klieber C, Shalagatskyi V, Temnov V V, Makarov D, Baek S-H, Eom C-B and Nelson K A 2013 Measurement of shorter-than-skin-depth acoustic pulses in a metal film via transient reflectivity *Appl. Phys. Lett.* **103** 173104

[92] van Capel P J S, Péronne E and Dijkhuis J I 2015 Nonlinear ultrafast acoustics at the nano scale *Ultrasonics* **56** 36–51

[93] Behari J and Tripathi B B 1970 Phonon dispersion in noble metals *J. Phys. C: Solid State Phys.* **3** 659–64

[94] Hiki Y and Granato A V 1966 Anharmonicity in noble metals; higher order elastic constants *Phys. Rev.* **144** 411–9

[95] Tang X and Fultz B 2011 First-principles study of phonon linewidths in noble metals *Phys. Rev.* B **84** 054303

[96] van Capel P J S and Dijkhuis J I 2010 Time-resolved interferometric detection of ultrafast strain solitons in sapphire *Phys. Rev.* B **81** 144106

[97] Maris H J and Tamura S 2011 Propagation of acoustic phonon solitons in nonmetallic crystals *Phys. Rev.* B **84** 024301

[98] Bojahr A, Herzog M, Schick D, Vrejoiu I and Bargheer M 2012 Calibrated real-time detection of nonlinearly propagating strain waves *Phys. Rev.* B **86** 144306

[99] Pezeril T, Klieber C, Shalagatskyi V, Vaudel G, Temnov V V, Schmidt O G and Makarov D 2014 Femtosecond imaging of nonlinear acoustics in gold *Opt. Express* **22** 4590–8

[100] Zhao H B, Fan Y, Lüpke G, Hanbicki A T, Li C H and Jonker B T 2011 Detection of coherent acoustic phonons by time-resolved second-harmonic generation *Phys. Rev.* B **83** 2012302

[101] Bykov A Y, Murzina T V, Olivier N, Wurtz G A and Zayats A V 2015 Coherent lattice dynamics in topological insulator Bi_2Te_3 probed with time-resolved optical second-harmonic generation *Phys. Rev.* B **92** 064305

[102] Huber L *et al* 2015 Coherent acoustic perturbation of second-harmonic generation in NiO *Phys. Rev.* B **92** 094304

[103] Melnikov A, Razdolski I, Wehling T O, Papaioannou E T, Roddatis V, Fumagalli P, Aktsipetrov O, Lichtenstein A I and Bovensiepen U 2011 Ultrafast transport of laser-excited spin-polarized carriers in Au/Fe/MgO(001) *Phys. Rev. Lett.* **107** 076601

[104] Wang F X, Rodriguez F J, Albers W M, Ahorinta R, Sipe J E and Kauranen M 2009 Surface and bulk contributions to the second-order nonlinear optical response of a gold film *Phys. Rev.* B **80** 233402

[105] McPeak K M, Jayanti S V, Kress S J P, Meyer S, Iotti S, Rossinelli A and Norris D J 2015 Plasmonic films can easily be better: Rules and recipes *ACS Photon.* **2** 326–33

[106] Lee C H, He H, Lamelas F, Vavra W, Uher C and Clarke R 1989 Epitaxial Co–Au superlattices *Phys. Rev. Lett.* **62** 653

[107] Yabuhara O, Ohtake M, Nukaga Y and Futamoto M 2011 Preparation and characterization of Co epitaxial thin films on Al_2O_3(0001) single-crystal substrates *J. Phys.: Conf. Ser.* **266** 012049

[108] Brandenburg J, Hhne R, Schultz L and Neu V 2009 Domain structure of epitaxial Co films with perpendicular anisotropy *Phys. Rev.* B **79** 054429
[109] den Broeder F J A, Kuiper D, van de Mosselaer A P and Hoving W 1988 Perpendicular magnetic anisotropy of Co–Au multilayers induced by interface sharpening *Phys. Rev. Lett.* **60** 2769
[110] Yamane H, Maeno Y and Kobayashi M 1993 Annealing effects on Co/noble metal multilayer films *J. Magn. Magn. Mater.* **126** 320–2
[111] Gubbiotti G, Carlotti G, Albertini F, Casoli F, Bontempi E, Depero L E, Kood H and Gomez R D 2003 Influence of annealing on Co/Au multilayers: a structural and magnetic study *Thin Solid Films* **428** 102
[112] Kirilyuk A, Kimel A V and Rasing T 2010 Ultrafast optical manipulation of magnetic order *Rev. Mod. Phys.* **82** 2731
[113] Rudolf D *et al* 2012 Ultrafast magnetization enhancement in metallic multilayers driven by superdiffusive spin current *Nat. Commun.* **3** 1037
[114] Vodungbo B *et al* 2016 Indirect excitation of ultrafast demagnetization *Sci. Rep.* **6** 18970
[115] Radu I *et al* 2011 Transient ferromagnetic-like state mediating ultrafast reversal of antiferromagnetically coupled spins *Nature* **472** 205–8
[116] Ostler T A *et al* 2012 Ultrafast heating as a sufficient stimulus for magnetization reversal in a ferrimagnet *Nat. Commun.* **3** 666
[117] Zhang Q, Nurmikko A V, Anguelouch A, Xiao G and Gupta A 2002 Coherent magnetization rotation and phase control by ultrashort optical pulses in CrO_2 thin films *Phys. Rev. Lett.* **89** 177402
[118] Bigot J-Y, Vomir M, Andrade L H F and Beaurepaire E 2005 Ultrafast magnetization dynamics in ferromagnetic cobalt: the role of anisotropy *Chem. Phys.* **76** 137–46
[119] Scherbakov A V, Salasyuk A S, Akimov A V, Liu X, Bombeck M, Brueggeman C, Yakovlev D R, Sapega V F, Furdyna J K and Bayer M 2010 Coherent magnetization precession in ferromagnetic (Ga,Mn)As induced by picosecond acoustic pulses *Phys. Rev. Lett.* **105** 117204
[120] Thevenard L, Perrone E, Gourdon C, Testelin C, Cubukcu M, Charron E, Vincent S, Lemaitre A and Perrin B 2010 Effect of picosecond strain pulses on thin layers of the ferromagnetic semiconductor (Ga,Mn)(As,P) *Phys. Rev.* B **82** 104422
[121] Kim J W, Vomir M and Bigot J-Y 2012 Ultrafast magneto-acoustics in nickel films *Phys. Rev. Lett.* **109** 166601
[122] Nelson K A, Miller R J D, Lutz D R and Fayer M D 1982 Optical generation of tunable ultrasonic waves *J. Appl. Phys.* **53** (1144)
[123] Janusonis J, Chang C L, van Loosdrecht P H M and Tobey R I 2015 Frequency tunable surface magneto elastic waves *Appl. Phys. Lett.* **106** 181601
[124] Janusonis J, Chang C L, Jansma T, Gatilova A, Lomonosov A M, Shalagatskyi V, Vlasov V S, Temnov V V and Tobey R I 2016 Ultrafast magnetoelastic probing of surface acoustic transients *Phys. Rev.* B **94** 024415
[125] Afanasiev D, Razdolski I, Skibinsky K M, Bolotin D, Yagupov S V, Strugatsky M B, Kirilyuk A, Rasing T and Kimel A V 2014 Laser excitation of lattice-driven anharmonic magnetization dynamics in dielectric $FeBO_3$ *Phys. Rev. Lett.* **112** 147403
[126] Kovalenko O, Pezeril T and Temnov V V 2013 New concept for magnetization switching by ultrafast acoustic pulses *Phys. Rev. Lett.* **110** 266602
[127] Thevenard L, Duquesne J-Y, Peronne E, von Bardeleben H J, Jaffres H, Ruttala S, George J-M, Lemaitre A and Gourdon C 2013 Irreversible magnetization switching using surface acoustic waves *Phys. Rev.* B **87** 144402
[128] Sampath V, Souza N, Bhattacharya D, Atkinson G M, Bandyopadhyay S and Atulasimha J 2016 Switching the magnetization of magnetostrictive nanomagnets from single-domain to non-volatile vortex states with a surface acoustic wave arXiv:1601.02081
[129] Sotier F, Thomay T, Hanke T, Korger J, Mahapatra S, Frey A, Brunner K, Bratschitsch R and Leitenstorfer A 2009 Femtosecond few-fermion dynamics and deterministic single-photon gain in a quantum dot *Nat. Phys.* **5** 352–6
[130] Efros Al L, Rosen M, Kuno M, Nirmal M, Norris D J and Bawendi M 1996 Band-edge exciton in quantum dots of semiconductors with a degenerate valence band: dark and bright exciton states *Phys. Rev.* B **54** 4843
[131] Huneke J, D'Amico I, Machnikowski P, Thomay T, Bratschitsch R, Leitenstorfer A and Kuhn T 2011 Role of coulomb correlations for femtosecond pump-probe signals obtained from a single quantum dot *Phys. Rev.* B **84** 115320
[132] Zurita-Sánchez J R and Novotny L 2002 Multipolar interband absorption in a semiconductor quantum dot: I. Electric quadrupole enhancement *J. Opt. Soc. Am.* B **19** 1355–62
[133] de Roo T, Haase J, Keller J, Hinz C, Schmid M, Seletskiy D V, Colfen H, Leitenstorfer A and Mecking S 2014 A direct approach to organic/inorganic semiconductor hybrid particles via functionalized polyfluorene ligands *Adv. Funct. Mater.* **24** 2714
[134] Alivisatos A P 1996 Perspectives on the physical chemistry of semiconductor nanocrystals *J. Phys. Chem.* **100** 13226–39
[135] Aktsipetrov O A, Kim E M, Kapra R V, Murzina T V, Kravets A F, Inoue M, Kuznetsova S V, Ivanchenko M V and Lifshits V G 2006 Magnetization-induced optical third-harmonic generation in Co and Fe nanostructures *Phys. Rev.* B **73** 140404
[136] Hanke T, Krauss G, Träutlein D, Wild B, Bratschitsch R and Leitenstorfer A 2009 Efficient nonlinear light emission of single gold optical antennas driven by few-cycle near-infrared pulses *Phys. Rev. Lett.* **103** 257404
[137] Hanke T, Cesar J, Knittel V, Trügler A, Hohenester U, Leitenstorfer A and Bratschitsch R 2012 Tailoring spatiotemporal light confinement in single plasmonic nanoantennas *Nano Lett.* **12** 992–6
[138] Brida D, Krauss G, Sell A and Leitenstorfer1 A 2014 Ultrabroadband Er:fiber lasers *Laser Photon Rev.* **8** 409–28